Physics of the Earth and Planetary Interiors 176 (2009) 1–18

Contents lists available at ScienceDirect

Physics of the Earth and Planetary Interiors

journal homepage: www.elsevier.com/locate/pepi

Searching for models of thermo-chemical convection that explain probabilistic tomography. II—Influence of physical and compositional parameters

Frédéric Deschamps*, Paul J. Tackley

Institute of Geophysics, Swiss Federal Institute of Technology Zurich, HPP L8.1, 8093 Zurich, Switzerland

ARTICLE INFO

Article history:
Received 13 May 2008
Received in revised form 11 February 2009
Accepted 6 March 2009

Keywords:
Thermo-chemical convection
Mantle structure and composition
Probabilistic tomography

ABSTRACT

We continue the exploration of the model space of thermo-chemical convection that we started in a previous study [Deschamps, F., Tackley, P.J., 2008. Exploring the model space of thermo-chemical convection. I—Principles and influence of the rheological parameters. Phys. Earth Planet. Inter. 171, 357–373]. In this second part, we study the influence of the Rayleigh number, the internal heating, the Clapeyron slope of the 660-km transition, the chemical density contrast between dense and regular materials (buoyancy ratio), and the volume fraction of dense material. We apply the same analysis and test the chemical and thermal density distributions predicted by various thermo-chemical models against those predicted by probabilistic tomography. Varying the reference Rayleigh number within a reasonable range of values for the Earth's mantle, we find significant differences in the flow pattern and efficiency of mixing. A Rayleigh number equal to 1/3 only of the standard value (10^8) helps to maintain compositional anomalies throughout the system during a long period of time. The internal heating has no or very little influence on the flow pattern and the efficiency of mixing. An endothermic phase transition with a (non-)dimensional Clapeyron slope lower than −1.0 MPa/K strongly inhibits the mass exchange and thus the efficiency of mixing. It provides a convenient way to maintain strong compositional anomalies in the lower mantle during a long period of time. The stability of the layer of dense material is mainly controlled by the buoyancy ratio, and the influence of the volume fraction of dense material is only of second order. These experiments, together with those performed in our previous study, suggest that four ingredients may enter a successful thermo-chemical model of convection for the Earth's mantle: (1) A buoyancy ratio between 0.15 and 0.25, which is equivalent to a chemical density contrast in the range 90–150 kg/m^3; (2) a large ($\geq 10^4$), thermal viscosity contrast, which creates and maintains pools of dense material at the bottom of the mantle; (3) a viscosity contrast at $d = 660$ km around 30; and (4) a Clapeyron slope of the phase transition at $d = 660$ km of about −3.0 to −1.5 MPa/K. In addition, pools of dense material can be generated and maintained for a large range of values of the chemical viscosity contrast, but the detailed structure of the pools significantly depends on this parameter.

1. Introduction

Because the Earth's mantle includes numerous complexities and uncertain parameters, the model space of mantle convection is huge. Comparisons against observational constraints (mainly from seismology, mineral physics, and geochemistry), reduce the size of the space of possible models, but so far no consensus could be reached on a successful model. Recently, a number of studies pointed out that seismological observations are not fully explained by temperature variations alone (Karato and Karki, 2001; Saltzer et al., 2001; Deschamps and Trampert, 2003; Trampert et al., 2004). The strong density variations observed in the lower mantle (Ishii and Tromp, 1999; Trampert et al., 2004) might be partly compositional in origin. A successful model of mantle convection (in the sense that it fits seismological observations) must therefore predict strong lateral variations of composition in the lower mantle, and maintain them over long periods of time. In a companion paper (Deschamps and Tackley, 2008), we started an extensive search in the model space of thermo-chemical convection to identify ingredients that are needed to maintain compositional anomalies in the lower mantle, and found that a moderate compositional viscosity ratio and a strongly temperature dependent viscosity are two of these ingredients. In the present paper, we continue this search and explore the influence of physical (Rayleigh number, internal heating, 660-km phase transition) and compositional (buoyancy ratio and fraction of dense material) parameters.

The Rayleigh number, *Ra*, controls the vigor of convection. When complexities like variable viscosity and depth-dependent thermal

* Corresponding author. Tel.: +41 446336806; fax: +41 446331065.
E-mail address: frederic.deschamps@erdw.ethz.ch (F. Deschamps).

0031-9201/$ – see front matter © 2009 Elsevier B.V. All rights reserved.
doi:10.1016/j.pepi.2009.03.012

expansion are accounted for, the definition of the Rayleigh number is not trivial. One usually defines a reference Rayleigh number, Ra_S, using reference values (e.g., surface values) of the parameters. Of course, one expects the mixing between dense and regular materials to be more efficient with increasing Ra_S. Because of uncertainties in mantle properties (mainly its viscosity), however, possible values for the Rayleigh number of the Earth's mantle may vary within one order of magnitude, and it is important to quantify this effect.

In the case of purely thermal convection with mixed heating, increase in the amount of internal heating, H_C, is known to reduce the strength of the bottom thermal boundary layer (e.g., Travis and Olson, 1994; Sotin and Labrosse, 1999; McNamara and Zhong, 2005). Thermal plumes are less vigorous, and if internal heating is large enough they do not reach the top of the system. It is important to check whether similar effects are also observed in thermo-chemical convection.

The 660-km discontinuity is associated with the transformation of ringwoodite into perovskite and magnesio-wüstite, which has a negative Clapeyron slope. The effect of an endothermic phase transition on thermal convection has been extensively studied in various geometries (e.g., Christensen and Yuen, 1985; Machetel and Weber, 1991; Tackley et al., 1993, 1994; Solheim and Peltier, 1994; Yuen et al., 1994). An endothermic phase change strongly modifies the flow pattern, the main change being the reduction of mass exchange between the upper and lower mantle. There are however significant differences between the patterns observed by 2D- and 3D-simulations. The former predict intermittent layering with slab avalanches occurring from time to time. The later, on the contrary, predict that the flow is never completely layered, with slab avalanches occurring not necessarily at the same location, but at any time.

The two important compositional parameters are the buoyancy ratio B (i.e., the chemical density contrast between dense and regular material relatively to the total thermal density contrast), and the volume fraction of dense material, X. The buoyancy ratio controls the amplitude of the deformation of the dense layer (e.g., Davaille, 1999; McNamara and Zhong, 2004; Jaupart et al., 2007). Variations in B lead to different patterns, from a stable layer (large B), to a fully unstable layer (small B). Furthermore, analogical experiments (Jellinek and Manga, 2002) suggest that the presence of a dense layer at the bottom of the system controls the location of thermal plumes. Linear stability analysis and analogical experiments (Jaupart et al., 2007) and numerical experiments with spherical geometry (McNamara and Zhong, 2004) suggest that the effects of the volume fraction are of second order compared to those of the buoyancy ratio.

Gathering the results from these new series of experiments and from our companion paper, we identify sensitive parameters and their possible values for the Earth's mantle. Interestingly, these values are consistent with additional, independent geophysical constraints.

2. Numerical modeling and results analysis

2.1. Numerical modeling

As in our companion paper, numerical experiments are performed with a 3D-Cartesian version of STAG3D (Tackley, 1998a, 2002). All runs are stopped at non-dimensional time $t = 0.0106$,

Table 1
Parameters and scallings.

Parameter	Symbol	Value	Units	Non-dimensional
Non-dimensional parameters				
Reference Rayleigh number	Ra_S			10^6–10^9
Buoyancy ratio	B			0.1–0.5
Volume fraction of dense material	X			0.05–0.30
Initial thickness of the dense layer	h_{DL}			0.05–0.30
Surface dissipation number	Di_S			1.2
Volume average dissipative number	Di			0.43
Total internal heating	H_C	0–130	mW/m^2	0–50
Compositional heating ratio	RH_C	10		
Physical and thermo-dynamical parameters (dimensional)				
Acceleration of gravity	g	9.81	m s^{-2}	1.0
Mantle thickness	D	2891	km	1.0
Super-adiabatic temperature difference	ΔT_S	2500	K	1.0
Reference adiabat	T_{as}	1600	K	0.64
Surface density	ρ_S	3300	kg/m^3	1.0
Bottom density	ρ_{bot}	5115	kg/m^3	1.55
Density jump at $z = 660$ km	$\Delta\rho_{660}$	400	kg/m^3	0.1212
Surface thermal expansion	α_S	5.0×10^{-5}	K^{-1}	1.0
Surface thermal diffusivity	κ_S	6.24×10^{-7}	m^2 s^{-1}	1.0
Heat capacity	C_P	1200	J kg^{-1} K^{-1}	1.0
Surface conductivity	k_S	3.0	W m^{-1} K^{-1}	1.0
Surface Grüneisen parameter	γ_S	1.091		
Clapeyron slope at $z = 660$ km	Γ	−4.6 to 0.0	MPa/K	-1.2×10^{-1} to 0.0
Viscosity law				
Surface thermal viscosity	μ_S	1.6×10^{21}	Pa s	1.0
Viscosity ratio at $z = 660$ km	$R\mu_{660}$	30		
Compositional viscosity ratio	$R\mu_c$	10^{-2} [a]		
Thermal viscosity ratio	$R\mu_T$	1 [a]		
Vertical viscosity ratio	$R\mu_z$	10		
Dimensional scallings				
Velocity	v	1.0	cm/year	1468
Time	t	424	Gyr	1.0
Heat flux	Φ	2.6	mW/m^2	1.0
Internal heating rate	H	2.72×10^{-13}	W kg^{-1}	1.0

[a] Except for the combined models in Section 5, for which $R\mu_T = 10^6$, and $10^{-2} \leq R\mu_c \leq 10^2$.

which correspond to a dimensional time equal to 4.5 Gyr. The size of the box is $4 \times 4 \times 1$, with 128 points in each horizontal direction, and 64 points in vertical direction (the grid spacing is vertically refined at the top and bottom of the system). Resolution tests for STAG3D with particles tracers were performed by Tackley and King (2003). We performed additional tests for selected cases with vertical resolution up to 96 points, but did not find significant differences in the time evolution of thermo-chemical structures. In particular, for models with large thermal viscosity and endothermic phase transition at 660 km, large thermo-chemical pools are generated whatever the vertical resolution we considered, and survive convection.

The system is heated both from the bottom and from within, and the internal heating rate is varied between 0 and 50, which is equivalent to dimensional heat flow between 0 and 130 mW/m^2. We accounted for the possibility that the MORB source region is depleted in radiogenic elements by increasing the heating rate of dense material by a factor 10 ($RH_C = 10$). The mantle heating rate is then adjusted to obtained the prescribed total heat production. Compressibility induces additional sources and sinks of heat that are controlled by the dissipation number, Di. This number depends on the thermal expansion and thus varies with depth. In all our calculations, the surface and volume average values of the dissipation number are $Di_S = 1.2$ and $\langle Di \rangle = 0.43$, respectively.

The conservative equations require definition of reference radial profiles for the density, the thermal expansion, and the temperature. These profiles are calculated using appropriate thermodynamic relationships (Tackley, 1996, 1998a). Density and thermal expansion are scaled with respect to their surface value, and temperature with respect to the super-adiabatic temperature difference across the system ΔT_S (Table 1).

The viscosity depends on depth and composition, but not on temperature (except the combined models in Section 5, for which the thermal viscosity ratio is $R\mu_T = 10^6$). Viscosity increases exponentially with depth following $\mu(z) = \exp(2.303z)$ (i.e., a bottom to top contrast of $R\mu_z = 10$), and an additional contrast of $R\mu_{660} = 30$ is imposed at $d = 660$ km ($z = 0.228$). The dense material is less viscous than the regular material by two orders of magnitude (except, again, for the combined models, for which we considered various values of the compositional viscosity ratio). Because thermal expansion and viscosity are not uniform, the definition of the Rayleigh number is non-unique. In the present study, we prescribed a reference Rayleigh number, Ra_S, calculated from the surface values of density and thermal expansion (Table 1), and from the viscosity value at non-dimensional depth $z = 0$ and non-dimensional $T = 0.9$. We performed experiments for values of Ra_S in the range 10^6–10^9. This reference Rayleigh number does not vary with time. On the contrary, the effective Rayleigh number, measured in the well-mixed interior, is time-dependent. Because the viscosity increases with depth and the thermal expansion decreases with depth, this Rayleigh number is smaller than Ra_S.

The compositional field is modeled with a collection of particle tracers (Tackley and King, 2003). We defined two types of particles, for dense and regular material, respectively, and used a total of 10

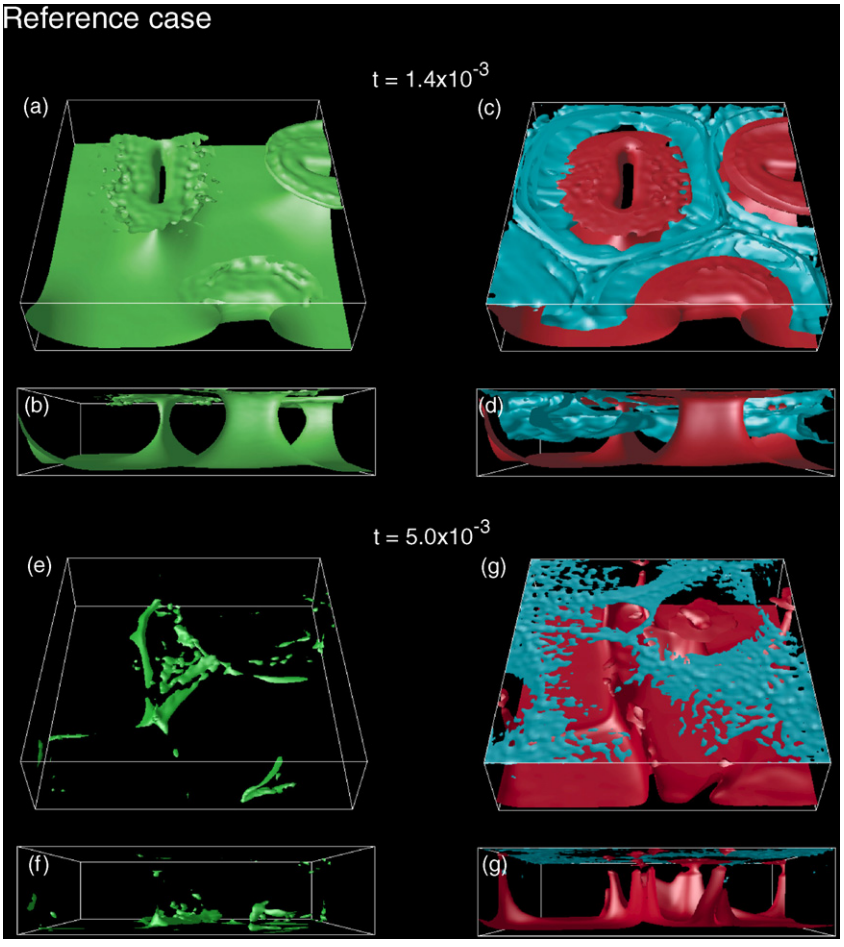

Fig. 1. Two snapshots of the reference case. (a–d) The 'piles' pattern, at $t = 1.4 \times 10^{-3}$ (0.6 Gyr). (e–h) A bit before the mixing time, at $t = 4.8 \times 10^{-3}$ (2.0 Gyr). (a, b and e, f) Isosurface of the concentration in dense particle, with contour level $C = 0.5$. (c, d and g, h) Isosurfaces of the non-dimensional temperature (relative to average), with contour levels $T - \langle T \rangle = -0.15$ (blue) and $T - \langle T \rangle = 0.15$ (red). (For interpretation of the references to color in this figure legend, the reader is referred to the web version of the article.)

million particles in each experiment. The fraction of dense material, X, is controlled by prescribing the fraction of dense particles. We varied this parameter between 5 and 30%. The compositional field is obtained by calculating the concentration C of dense particles in each cell. C varies between 0 for a cell filled with regular material only, and 1 for a cell filled with dense particle only. Dense particles are initially concentrated at the bottom of the box in a layer of non-dimensional thickness h_{DL}. For geometrical reasons, h_{DL} is numerically equal to the initial volume fraction of dense material, X. The density difference between the dense and regular materials is controlled by the buoyancy ratio:

$$B \equiv \frac{\Delta\rho_c(z)}{\alpha_S \rho_z \, \Delta T_S}, \tag{1}$$

where α_S is the thermal expansion at zero pressure, and ρ_z is the average density at depth z, and ΔT_S is the super-adiabatic temperature difference across the system. The chemical density contrast creates a negative buoyancy that opposes the positive buoyancy due to the thermal density contrast $\Delta\rho_T = \alpha_S \rho_z \, \Delta T_S$. We carried out experiments for buoyancy ratios between 0.1 and 0.5. Taking $\alpha_S = 5.0 \times 10^{-5}\,\mathrm{K}^{-1}$, $\rho_{bot} = 5115\,\mathrm{kg/m^3}$ (value at the bottom of the system) and $\Delta T_S = 2500\,\mathrm{K}$, the density contrast between dense and regular material thus varies between 64.0 and 320.0 kg/m^3.

The 660-km phase change is modeled with a discontinuous phase transition that is controlled by defining a point on the phase boundary and a Clapeyron slope, Γ. We imposed $z = 660\,\mathrm{km}$ and $T = 1900\,\mathrm{K}$ as anchor point, and varied the Clapeyron slope between −3.2 and 0 MPa/K. The Clapeyron slope is scaled with

$$\Gamma_0 = \frac{\rho_S g D}{\Delta T_S}, \tag{2}$$

where g is the gravity acceleration and D is the mantle thickness. Taking $\rho_S = 3300\,\mathrm{kg/m^3}$ and $\Delta T_S = 2500\,\mathrm{K}$, we have $\Gamma_0 = 38.2\,\mathrm{MPa/K}$. The density contrast at the phase transition is $\Delta\rho_{660} = 400\,\mathrm{kg/m^3}$ and is scaled with the surface density. A measure of the strength of the phase transition is the phase buoyancy ratio P, i.e. the ratio of the buoyancy induced by the phase transition to the thermal buoyancy:

$$P = \frac{(\Gamma \, \Delta T_{pt} \, \Delta\rho_{pt})/\rho_{pt} g D}{\alpha_{pt} \rho_{pt} \, \Delta T_{pt}} = \frac{\Gamma \, \Delta\rho_{pt}}{\alpha_{pt} \rho_{pt}^2 g D}, \tag{3}$$

where α_{pt}, ρ_{pt}, $\Delta\rho_{pt}$, and ΔT_{pt}, are the thermal expansion, density, density jump, and temperature difference at the phase transition. The thermodynamic reference model we used indicate that $\alpha_{660}/\alpha_S = 0.44$ and $\rho_{660}/\rho_S = 0.12$. Taking $\alpha_S = 5.0 \times 10^{-5}\,\mathrm{K}^{-1}$, $\rho_S = 3300\,\mathrm{kg/m^3}$, and $\Delta\rho_{660} = 400\,\mathrm{kg/m^3}$, the range of values of Clapeyron slope we explored leads to values of P between −0.04 and 0.

The thermal initial condition consists in superposing random anomalies of temperature to a geotherm issued from 2D calculations with similar properties to the 3D ones. This allows reducing the transient phase during which the dense layer heats up, and has only small consequences on our calculations. In the reference case (see below), for instance, the onset of instability of the dense layer is slightly delayed in time and thermo-chemical plumes are slightly less vigorous.

2.2. Results analysis

We focused our analysis on the mapping of thermal and chemical anomalies and their time evolution. These are of course closely related to the flow pattern. Our analysis is based on several observations.

First, model parameters influence the stability of the bottom layer of dense material. We estimated the time for the onset of instability of this layer (t_{onset}) from the average depth of dense material, $\langle h_C \rangle$, which varies between $h_{DL}/2$ (numerically equal to $X/2$, where X is the initial volume fraction of dense material) for a stable layer, and 1/2 for a well-mixed system. A sharp increase of $\langle h_C \rangle$ from its initial value $X/2$ clearly indicates that the dense layer became unstable.

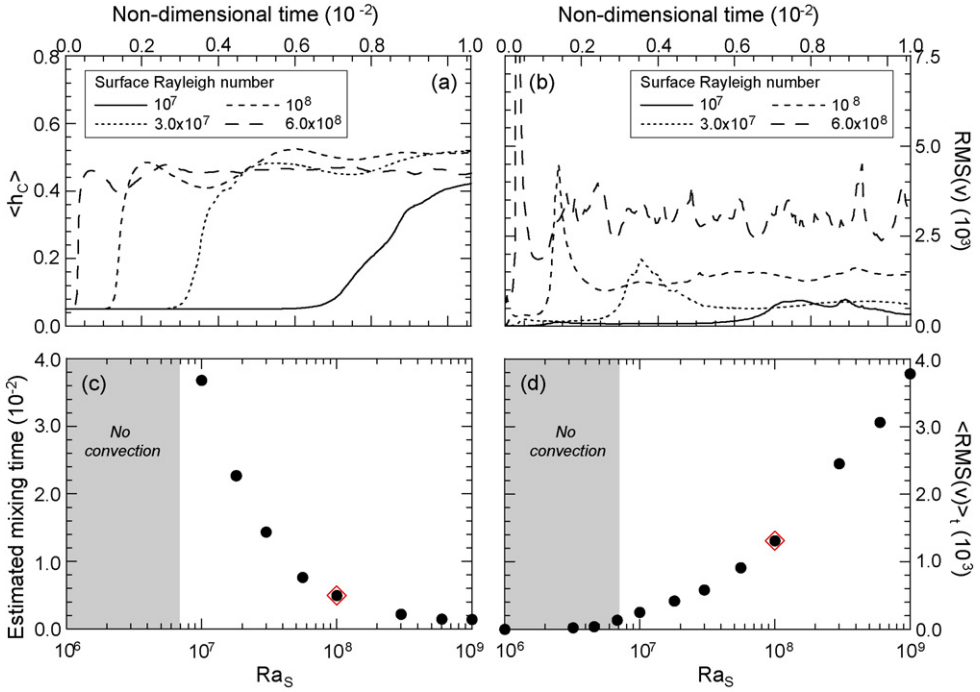

Fig. 2. Influence of the reference Rayleigh number, Ra_S. (a) Average depth of dense material, $\langle h_C \rangle$, as a function of time and for various values of Ra_S. (b) RMS of the flow velocity as a function of time and for various values of Ra_S. (c) Estimated mixing time as a function of Ra_S. (d) Time average RMS of the flow velocity as a function of Ra_S. Note that for $Ra_S \leq 7.0 \times 10^6$, the whole system remain stable during the entire duration of the run. In plots (c) and (d), the reference case is indicated by the red diamond. (For interpretation of the references to color in this figure legend, the reader is referred to the web version of the article.)

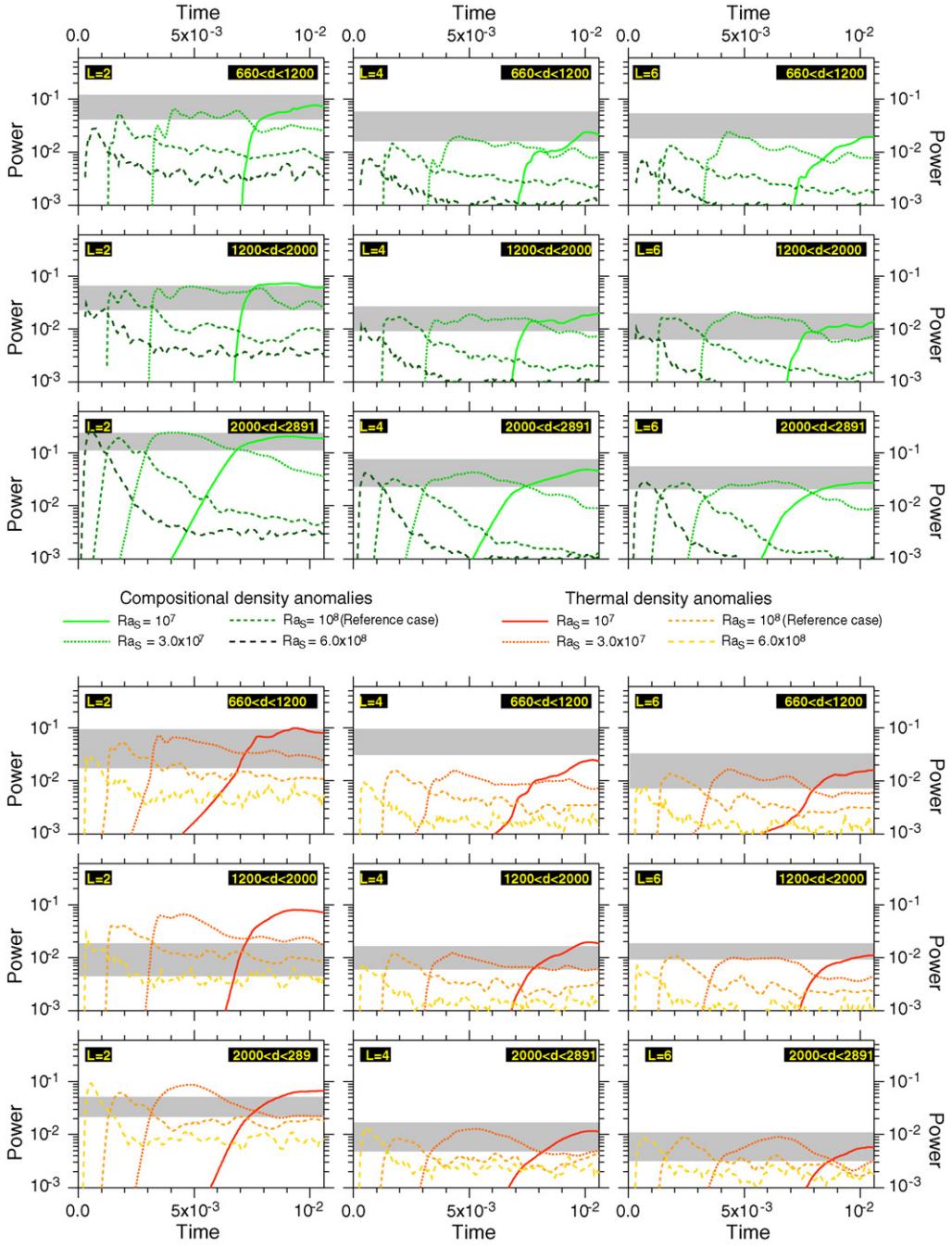

Fig. 3. Power of chemical (three top rows) and thermal (three bottom rows) density anomalies as a function of time and for various values of the reference Rayleigh number, Ra_S. Anomalies are averaged within three layers ($660 \le d \le 1200$ km, $1200 \le d \le 2000$ km, and $2000 \le d \le 2891$ km), and we considered three spherical harmonics ($L=2$, $L=4$, and $L=6$). Gray bands indicate the power spectrum predicted by RT246g within twice its standard deviation.

We then estimated the mixing time from the evolution of the variance in the compositional field, var(t). First, we calculated the time integral:

$$E = \int_0^{t_{\mathrm{run}}} \left[1 - \frac{\mathrm{var}(t)}{\mathrm{var}(t=0)}\right] \mathrm{d}t, \tag{4}$$

where t_{run} is the run duration. The function $e(t) = 1 - \mathrm{var}(t)/\mathrm{var}(t=0)$ varies between 0 and its statistical limit:

$$e_{\max} = 1 - \frac{N-1}{n_{\mathrm{part}}}, \tag{5}$$

where n_{part} and N are the number of particle tracers and the number of cells, respectively. We then compared the integral E to that of the function:

$$g\left(\frac{t_0}{t}\right) = e_{\max}\xi^2 \frac{\exp(\xi)}{[\exp(\xi)-1]^2}, \tag{6}$$

where $\xi = (t_0/t)^{1.5}$, and t_0 is the time at which $g(\xi)$ reaches 92% of its maximum value, $e_{\max}$ (Eq. (5)). The reason we modeled $e(t)$ with $g(\xi)$ is briefly discussed in our companion paper (Deschamps and Tackley, 2008). The mixing time t_{mix} is finally defined as the value of t_0 that fits Eq. (4) at best. This approach allows estimates of the mixing time even if mixing is not completed before t_{run}. In cases for which mixing is completed before t_{run}, the calculated mixing time agrees well with the observed time at which $e(t)$ reaches 92% of its statistical limit (Deschamps and Tackley, 2008). However, when mixing is strongly inhibited, our approach poorly estimates the

mixing time. Such cases include models with large ($\geq$0.35) values of the buoyancy ratio, for which the dense layer remains stable, and models with large values of the 660-km transition Clapeyron slope, for which dense material is filtered at $d = 660$ km.

An alternative measure of mixing efficiency is the time average of the average altitude of dense material, $\langle\overline{h_C}\rangle$, which varies between 1/2 (the dense and regular material are well mixed during the entire run) and $h_{DL}/2$ (the layer of dense material remain stable during the entire run). It is convenient to normalize this average altitude using its upper and lower bounds:

$$\zeta = \frac{2\langle\overline{h_C}\rangle - h_{DL}}{1 - h_{DL}} \quad (7)$$

The RMS of the flow velocity, RMS(v), and its time average, $\langle \mathrm{RMS}(v)\rangle_t$, provide good estimates of the amplitude of the flow velocity, and thus give indirect estimate of the mixing efficiency. Note that the bulk Lagrangian strain rate may also be used for similar purpose (Coltice, 2005). In most cases, the onset of instability is followed by a sharp increase in RMS(v), up to a maximum value that depends on the model parameters. RMS(v) then decreases again and oscillates around a constant value during the rest of the experiment.

At each time step, we calculate the lateral density anomalies due to lateral variations in temperature and composition. Thermal and chemical density anomalies are relative to radial density profiles derived from the radial profiles of temperature and composition, respectively. First order properties of the thermo-chemical structure of the flow, e.g., the presence of a stable layer of dense material, or two-layered convection, can be deduced from the radial profiles of average composition and temperature and of the RMS of density anomalies. Spectral heterogeneity maps (SHM) of chemical and thermal density anomalies provide more detailed information on this structure. Furthermore, to test our models of thermo-chemical convection against seismic tomography, we converted the Fourier power spectra of the density anomalies into spherical harmonics power spectra following Chevrot et al. (1998). These comparisons also require radial averaging of the convection models according to the vertical parameterization of the tomographic model (in our case, RT246g (Trampert et al., 2004), which includes three layers in the lower mantle).

2.3. Reference case

For comparison, we defined a reference case with the following properties. The mantle non-dimensional heating rate is equal to 25 (equivalent to a dimensional heat flow of 65 mW/m^2), and the Rayleigh number is equal to 10^8. The buoyancy ratio and volume fraction of dense material are $B = 0.2$ and $X = 10\%$, respectively. The Clapeyron slope of the 660-km transition is set to zero. Note that the parameters of the viscosity law are the same for all the calculations shown in this paper, with values listed in Table 1.

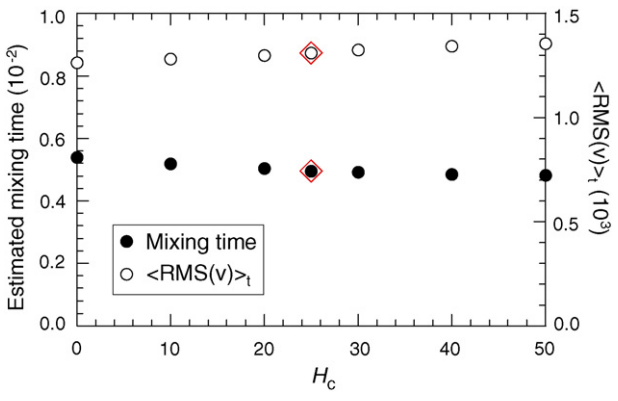

Fig. 4. Influence of internal heating, H_C. Plain and open circles show the estimated mixing time and the time average RMS of the flow velocity, respectively, as a function of H_C. The reference case is indicated by the red diamond. (For interpretation of the references to color in this figure legend, the reader is referred to the web version of the article.)

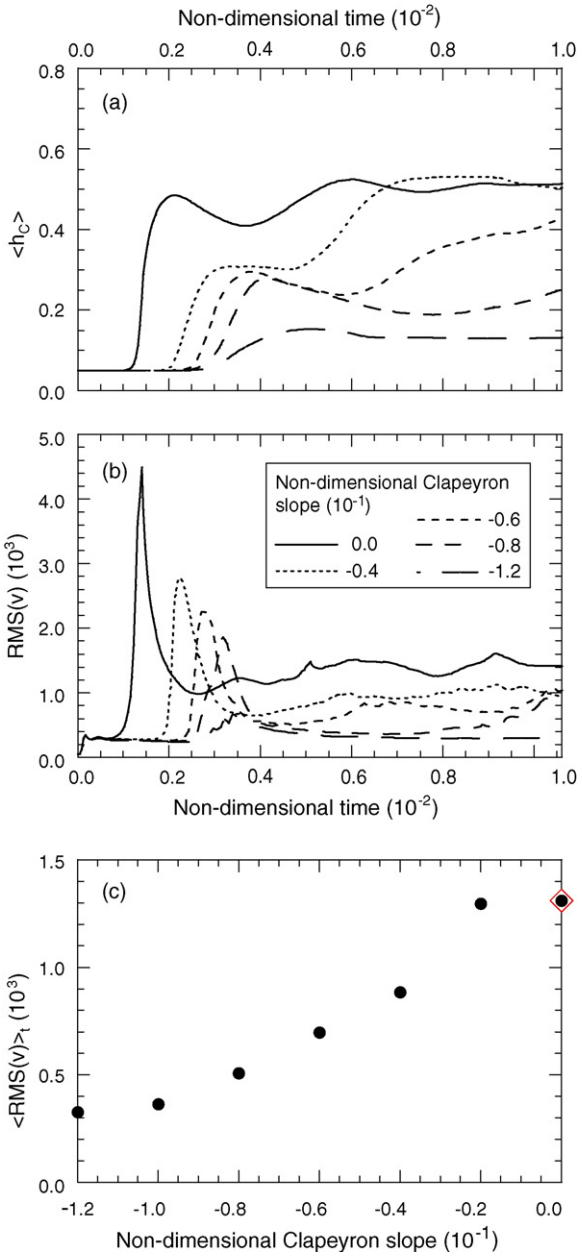

Fig. 5. Influence of the Clapeyron slope at $d = 660$ km, Γ_{660}. (a) Average depth of dense material, $\langle h_C\rangle$, as a function of time and for various values of Γ_{660}. (b) RMS of the flow velocity as a function of time and for various values of Γ_{660}. (c) Time average RMS of the flow velocity as a function of Γ_{660}. In plot (c), the reference case is indicated by the red diamond. (For interpretation of the references to color in this figure legend, the reader is referred to the web version of the article.)

After the onset of instability of the layer of dense material, at $t_{onset} \sim 0.9 \times 10^{-3}$ (0.4 Gyr), large thermo-chemical plumes rise from the dense layer and entrain dense material upwards (Fig. 1a–d). This 'piles' pattern explain probabilistic tomography well (Deschamps et al., 2007), but is short-lived, about $\delta t \sim 10^{-3}$ (0.4 Gyr) (Deschamps and Tackley, 2008). The thermal plumes, on the contrary, remain present until the end of the run. Dense and regular material quickly mix, with an estimated mixing time $t_{mix} = 5.0 \times 10^{-3}$ (2.1 Gyr) (Fig. 1e–h). As a result, the amplitude of

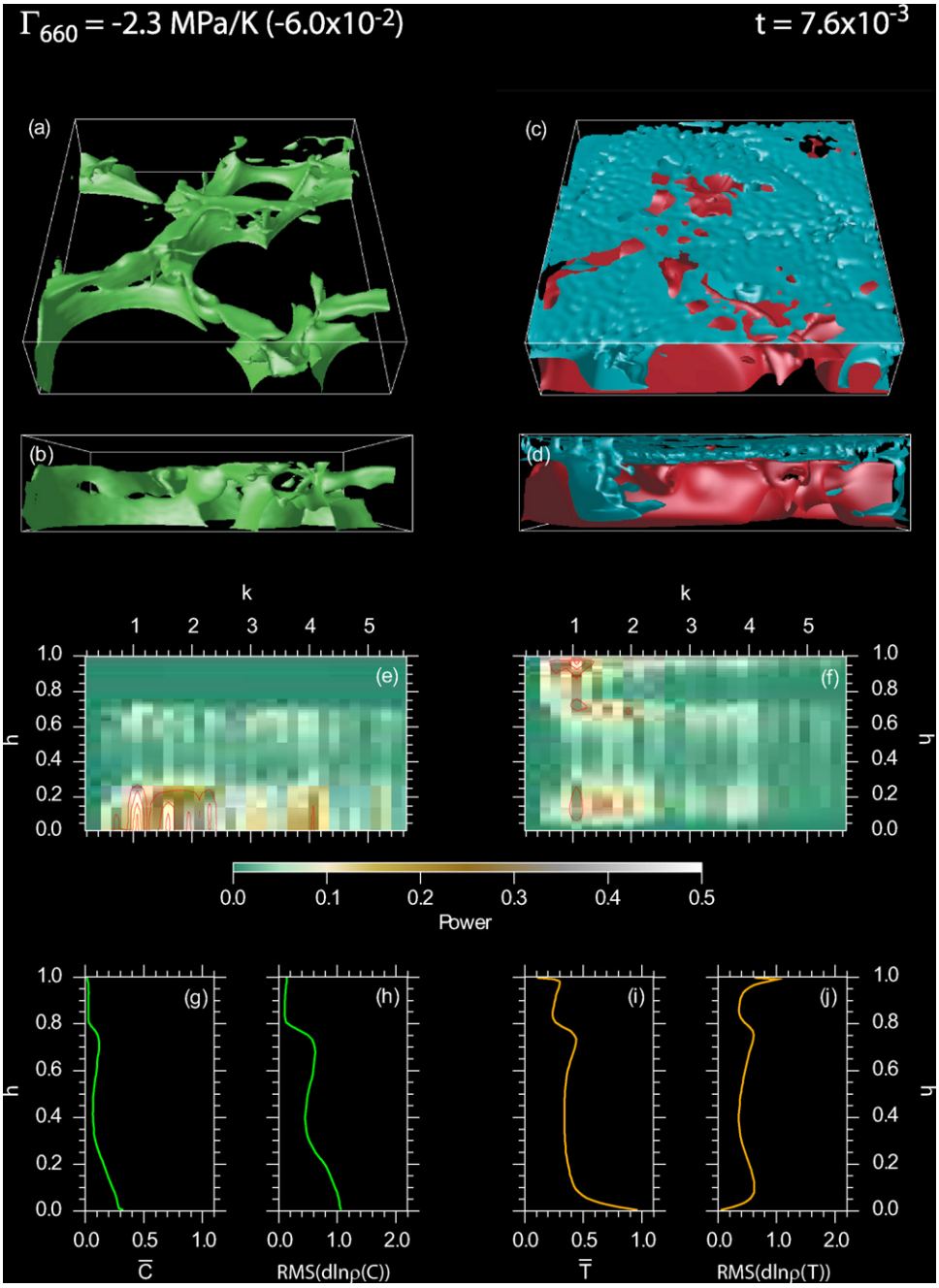

Fig. 6. Snapshot of the case $\Gamma_{660} = -2.3$ MPa/K (i.e., a non-dimensional value of -6.0×10^{-2}) at $t = 7.6 \times 10^{-3}$ (3.2 Gyr). Other parameters are $Ra_S = 10^8$, $H_C = 25$ (corresponding to $\Phi_{surf} = 65$ mW/m^2), $B = 0.2$, and $X = 10\%$. (a and b) Isosurface of the concentration in dense particle, with contour level $C = 0.5$. (c and d) Isosurfaces of the non-dimensional temperature (relative to average), with contour levels $T - \langle T \rangle = -0.15$ (blue) and $T - \langle T \rangle = 0.15$ (red). (e) Spectral heterogeneity map (SHM) of the chemical density anomalies, d ln ρ_c. (f) SHM of the thermal density anomalies, d ln ρ_T. SHMs are plotted with both a color scale and contour levels (red curves, interval is 0.2). h is the non-dimensional altitude. (g) Profile of the horizontally average concentration in dense particle, $\bar{C}$. (h) Profile of the RMS of the chemical density anomalies d ln ρ_c. (i) Profile of the horizontally average non-dimensional temperature, $\bar{T}$. (j) Profile of the RMS of the thermal density anomalies d ln ρ_T. (For interpretation of the references to color in this figure legend, the reader is referred to the web version of the article.)

the lateral variations of composition rapidly decreases with time. The reference case is thus unable to maintain lateral anomalies of composition over a long period of time.

3. Influence of physical parameters

3.1. Rayleigh number

We first explored the influence of the Rayleigh number, varying Ra_S between 10^6 and 10^9. As one would expect, the time for the onset of instability, t_{onset}, increases with decreasing Ra_S (Fig. 2a). If the prescribed Ra_S is too small, the whole layer remains stable during the entire run. Of course, the critical Rayleigh number depends on the input parameters, mainly the parameters of the viscosity law. For values similar to those of the reference case, we found that the critical Rayleigh number is around 7.0×10^6. This value may sound a bit large, but one may recall that the presence of dense material at the bottom of the system and the decrease of thermal expansion increase the stability of the system. Convection gets more vigorous with increasing Rayleigh number and unsurprisingly, the

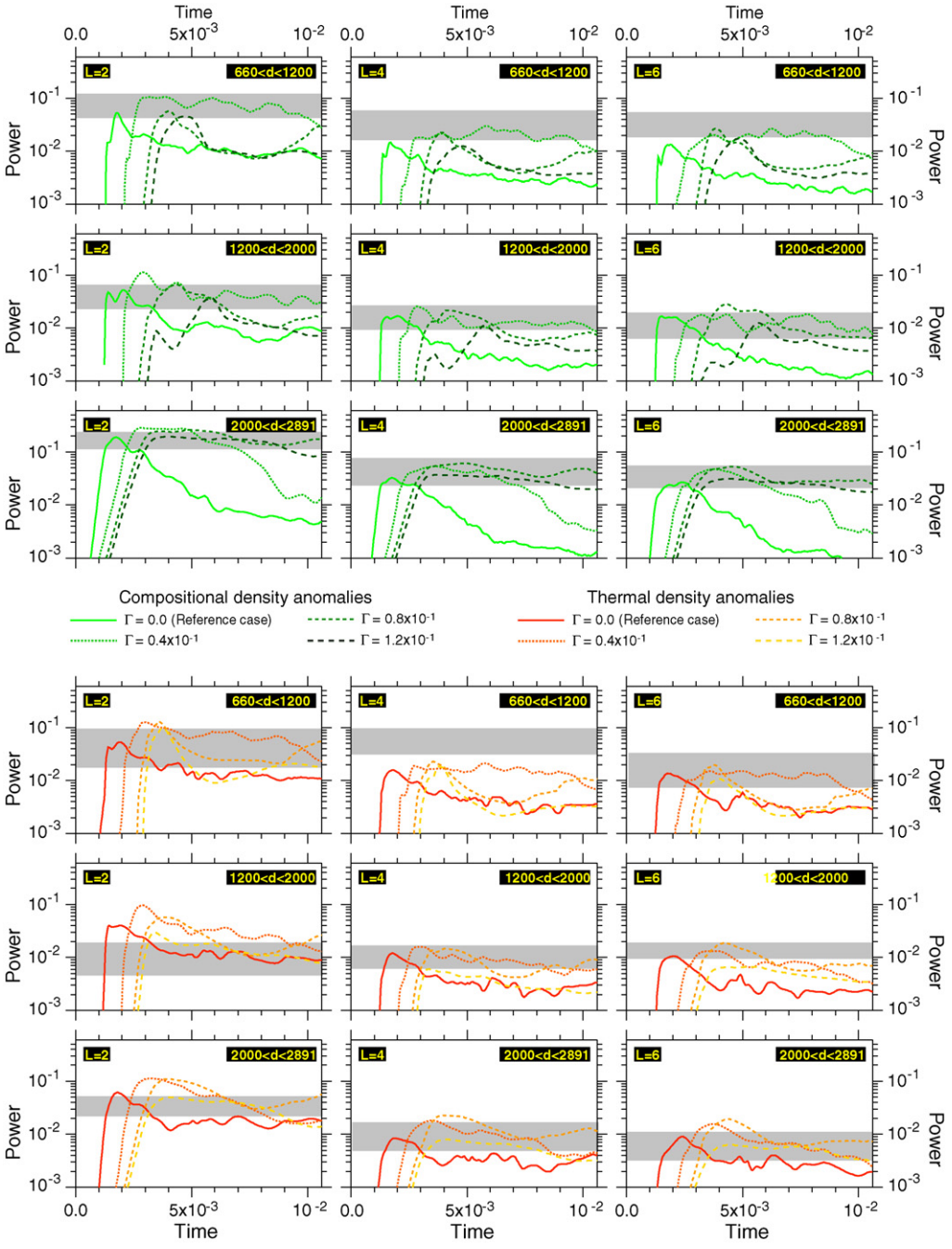

Fig. 7. Same as Fig. 3, but for various values of the Clapeyron slope at $z = 660$ km, Γ_{660}.

mixing between dense and regular material is more efficient (Fig. 2c and d). For instance, the values of the estimated mixing time, t_{mix}, and of the time average of the RMS of the velocities, $\langle \mathrm{RMS}(v) \rangle_t$, for $Ra_S = 6.0 \times 10^8$ are smaller than those for $Ra_S = 10^8$ (reference case) by a factors 4 and 2, respectively. As in the reference case, the onset of instability is followed by the rise of thermo-chemical plumes. The duration of this episode decreases with increasing Ra_S. Lateral variations of composition at low Ra_S are maintained during longer periods of time than at high Ra_S, and the power spectra of these compositional anomalies decreases with time more smoothly (Fig. 3).

A typical value of Ra_S for the Earth's mantle is 10^8. This value is derived from the data reported in Table 1, but due to uncertainties in some parameters (mainly, the uppermost mantle viscosity, thermal expansion and thermal diffusivity) it is reasonable to consider values of Ra_S between 3.0×10^7 and 3.0×10^8. The series of experiences presented in this section show that the efficiency of mixing significantly varies within this range of values. In particular, a value of Ra_S close to the lower bound (e.g., due to an upper mantle viscosity larger than the usual value by a factor 3) would help maintaining compositional anomalies in the lower mantle for a long period of time, and explain probabilistic tomography better.

3.2. Internal heating

We have then varied the amount of internal heating between 0 and 50 (equivalent to a heat flux of 130 mW/m^2), but did not find substantial differences depending on this parameter. For all the values of H_C we explored, the flow pattern and its time evolution are similar, with large thermo-chemical plumes generating early in

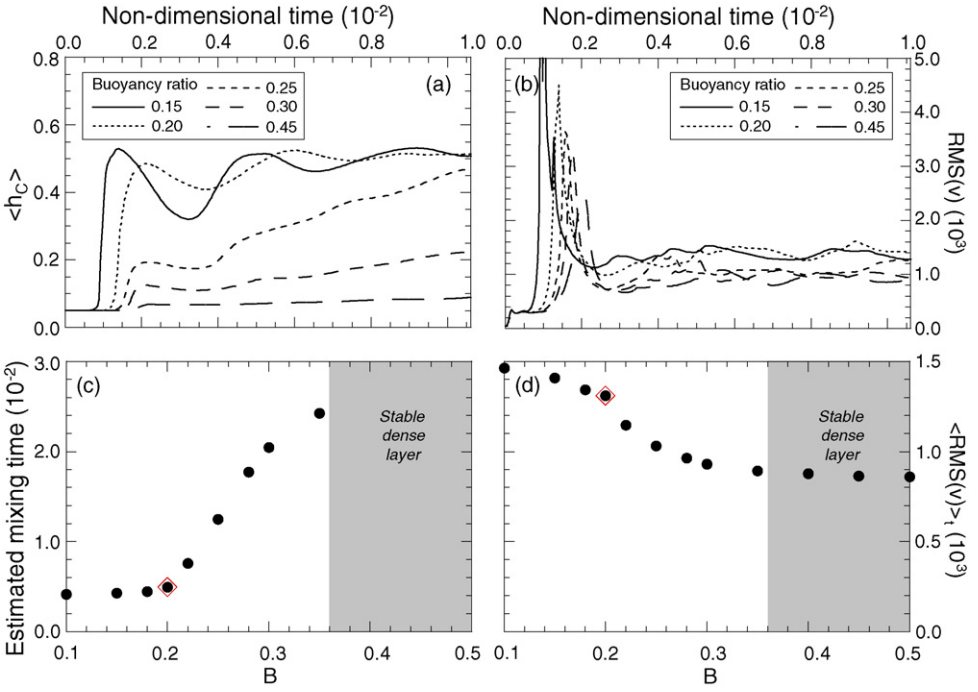

Fig. 8. Same as Fig. 2, but for various values of the buoyancy ratio, B.

the run history (see reference case). $\langle \mathrm{RMS}(v)\rangle_t$, is nearly constant with H_C (Fig. 4, open dots). Variations in t_{mix} with H_C are very small (Fig. 4, black dots), and mixing is efficient in all cases. We conducted additional experiments for buoyancy ratios $B = 0.1$ and 0.4 and three values of the internal heating (0, 25, and 50), and found that the variations in t_{mix} and $\langle \mathrm{RMS}(v)\rangle_t$ with H_C are still very small.

Numerical experiments of purely thermal convection in various geometries showed that the presence of internal heating strongly reduces the vigor of thermal plumes (Travis and Olson, 1994; Sotin and Labrosse, 1999; McNamara and Zhong, 2005). By contrast, the results of our experiments suggest that the amount of internal heating does not significantly influence thermo-chemical convection. This disagreement may be explained by the fact that part of the energy provided by internal heating is used as potential energy for the particles of dense material. In addition, because we imposed a compositional heating ratio (RH_C) of 10, part of internal heating may also be used to heat up the dense material. These explanations are consistent with the observation that the surface heat flow is smaller than the sum of the bottom and internal heating heat flows.

3.3. Phase transition at $z = 660$ km

We conducted numerical experiments with Clapeyron slope Γ_{660} of the phase transition at $d = 660$ km (i.e., a non-dimensional altitude $h = 0.771$) between −4.6 and 0 MPa/K (i.e., non-dimensional values between -1.2×10^{-1} and 0). In agreement with previous studies (Christensen and Yuen, 1985; Machetel and Weber, 1991; Tackley et al., 1993, 1994; Solheim and Peltier, 1994; Yuen et al., 1994), we find that the presence of an endothermic phase transition with low enough (≤ -1.5 MPa/K, i.e. a non-dimensional value of -4.0×10^{-2}) Clapeyron slope inhibits the mass exchange between the upper and lower layers. Furthermore, the RMS of velocity strongly decreases (Fig. 5, plots b and c). Consequently, mixing between dense and regular materials is much less efficient, as indicated by the time evolution of the average altitude of dense material, $\langle h_C\rangle$ (Fig. 5a). Note that the mixing time estimated by Eq. (4) is not accurate in this case, because the function $e(t) = 1 - \mathrm{var}(t)/\mathrm{var}(t = 0)$ do not fit Eq. (6) well.

The influence of phase transition on cold downwellings and on hot plumes is radically different. Cold downwellings are temporally stacked above the phase transition. When the mass of accumulated cold material is large enough, this accumulated material crosses the phase boundary and sinks to the bottom of the system. These avalanches are locally intermittent, but at any time of the run there is one occurring somewhere. The system is thus never fully stratified. Hot plumes rising from the bottom, on the contrary, are stopped below the phase transition, and smaller, secondary plumes are generated above the phase transition, as suggested by the temperature profile (Fig. 6i). The upward mass transfer is strongly inhibited, and most of the dense material remains trapped below the phase transition during a long period of time (Fig. 6, plots a and b). Filtering effects have been previously noted in 2D-Cartesian geometry (Weinstein, 1992). The dense material concentrates along hot ridges that interconnect the hot plumes, leading to large holes in the initial layer of dense material. Interestingly, the phase transition is not strictly impermeable and small amounts of dense material are entrained upwards by secondary plumes. Permeability increases with decreasing absolute value of the Clapeyron slope. In the case $\Gamma_{660} = -1.5$ MPa/K (-4.0×10^{-2}), for instance, mixing is nearly completed by the end of the run, as indicated by the time evolution of $\langle h_C\rangle$ (Fig. 5a). In the case $\Gamma_{660} = -2.3$ MPa/K (-6.0×10^{-2}), on the contrary, $\langle h_C\rangle$ only reaches 0.4 by the end of the run, meaning that dense material is distributed nearly completely below the phase transition.

An important consequence of trapping the dense material in the lower mantle is to create strong chemical density anomalies at the bottom of the system ($z \geq 0.85$), and moderate ones below the phase transition (Fig. 6, plots e and h). Moderate thermal density anomalies are also present at the bottom of the system and below the phase transition (Fig. 6, plots f and j), but the strongest thermal density anomalies are seen at the top of the system. These anomalies are maintained for a long period of time, and their power spectra fit very well those predicted by probabilistic tomography (Fig. 7), even in the layer 660–1200 km. Note however that a Clapeyron slope lower than −2.7 MPa/K (-7.0×10^{-2}) is not desirable because it keeps dense material at the very bottom of the system. As a con-

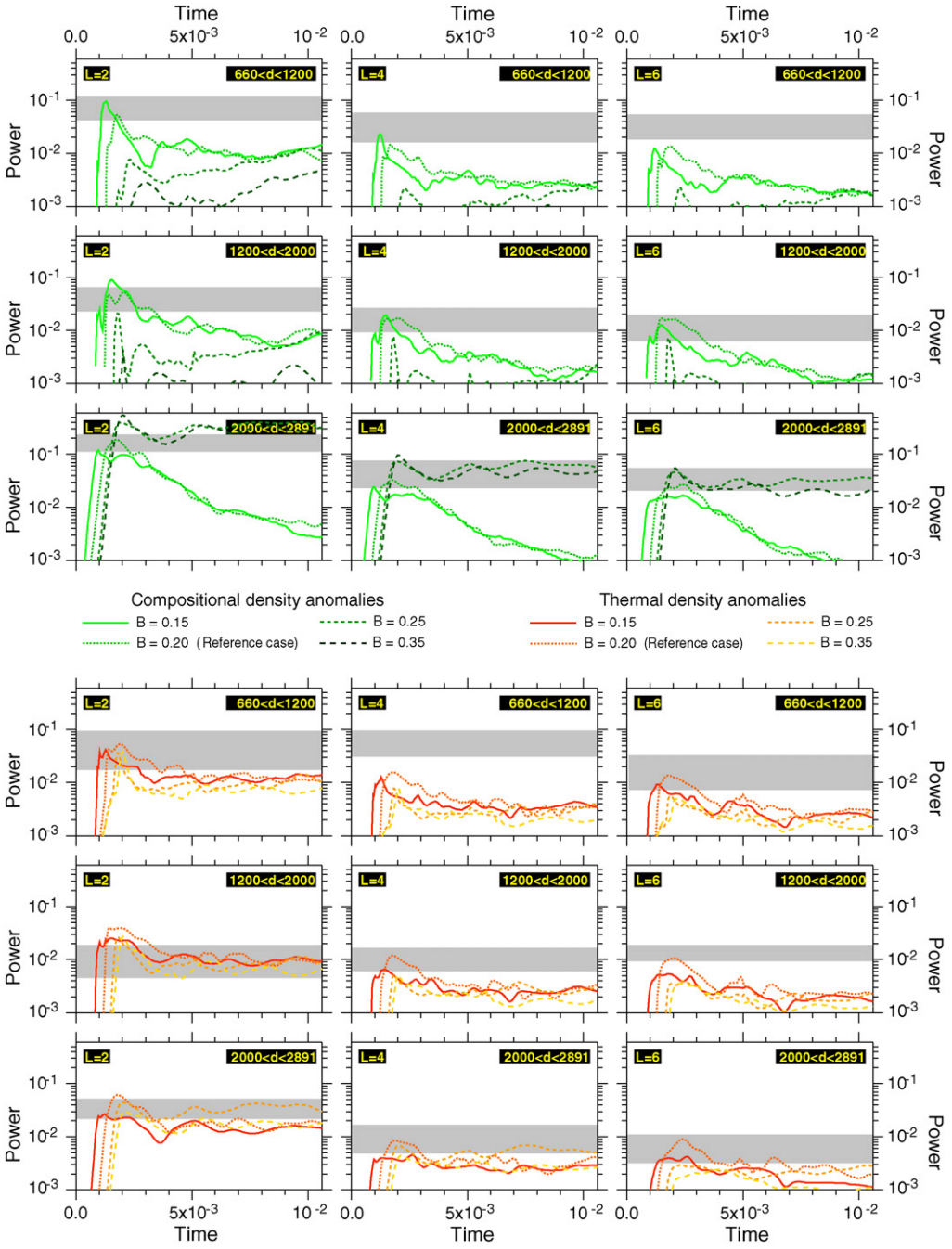

Fig. 9. Same as Fig. 3, but for various values of the buoyancy ratio, B.

sequence, the power of chemical density anomalies for depths in the range $0.23 \leq z \leq 0.85$ ($660 \leq d \leq 2500$ km) is small and does fit probabilistic tomography, even for spherical harmonic degree 2.

We did not account for the olivine to wadsleyite phase transition at the $d = 410$-km depth. Because this transition is exothermic, it may partly balances the effects of the 660-km transition. However, its phase buoyancy parameter is likely much smaller than that of the 660-km transition (assuming that this transition is well approximated by the transformation of ringwoodite into perovskite and magnesio-wüstite). First the amplitude of the Clapeyron slope 410-km phase transition is smaller than that of the 660-km phase transition, between 1.5 and 2.5 MPa/K (Katsura and Ito, 1989). Note that Bina and Helffrich (1994) proposed a slightly larger value, 3.0 MPa/K, i.e., comparable to that at 660-km. Second, the relative density jump at 410 km is only half that at 660 km. Finally, the thermal expansion decreases with depth, i.e. that the thermal buoyancy (for a given temperature change) is larger at 410 km than at 660 km. Numerical experiments (Tackley et al., 1994) confirmed that the effect of the 410-km phase transition are small compared to those of the 660-km transition.

4. Influence of compositional parameters

4.1. Buoyancy ratio

We varied the buoyancy ratio in the range 0.1–0.5, which according to the scalings in Table 1 is equivalent to density contrasts

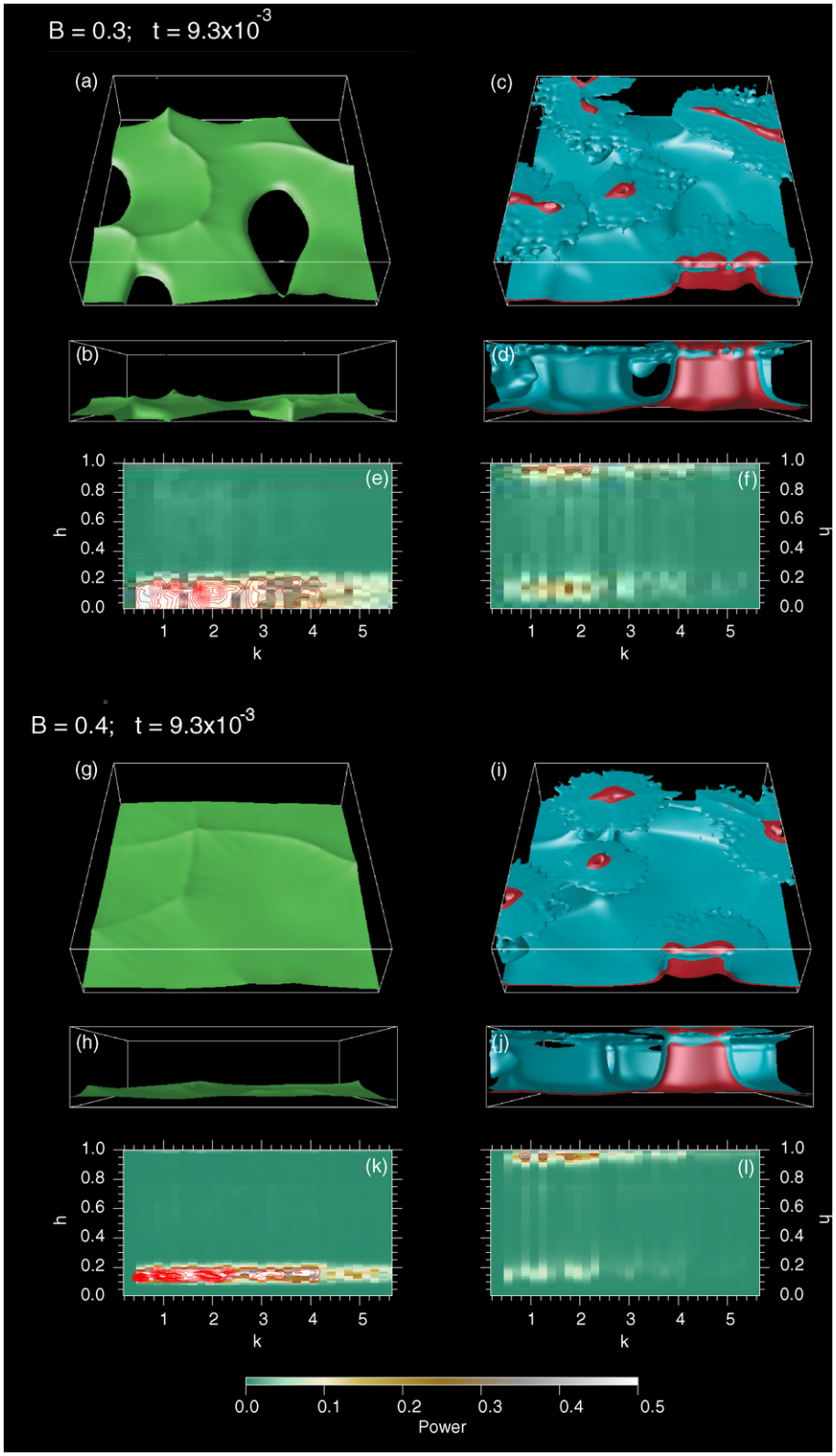

Fig. 10. (a–f) Snapshot of the case $B = 0.3$ at $t = 9.3 \times 10^{-3}$ (3.9 Gyr). Other parameters are as in the reference case ($Ra_S = 10^8$, $H_C = 25$, $X = 10\%$, and $\Gamma_{660} = 0$). (a and b) Isosurface of the concentration in dense particle, with contour level $C = 0.5$. (c and d) Isosurfaces of the non-dimensional temperature (relative to average), with contour levels $T - \langle T \rangle = -0.05$ (blue) and $T - \langle T \rangle = 0.05$ (red). (e) Spectral heterogeneity map (SHM) of the chemical density anomalies, $\mathrm{d} \ln \rho_C$. (f) SHM of the thermal density anomalies, $\mathrm{d} \ln \rho_T$. SHMs are plotted with both a color scale and contour levels (red curves, interval is 0.2). h is the non-dimensional altitude. (g–l) Snapshot of the case $B = 0.4$ at $t = 9.3 \times 10^{-3}$ (3.9 Gyr). Other parameters are as in the reference case ($Ra_S = 10^8$, $H_C = 25$, $X = 10\%$, and $\Gamma_{660} = 0$). Plots description is similar to that for plots (a–f). In plots (i) and (j), contour levels for temperature isosurfaces are $T - \langle T \rangle = -0.05$ (blue) and $T - \langle T \rangle = 0.05$ (red). (For interpretation of the references to color in this figure legend, the reader is referred to the web version of the article.)

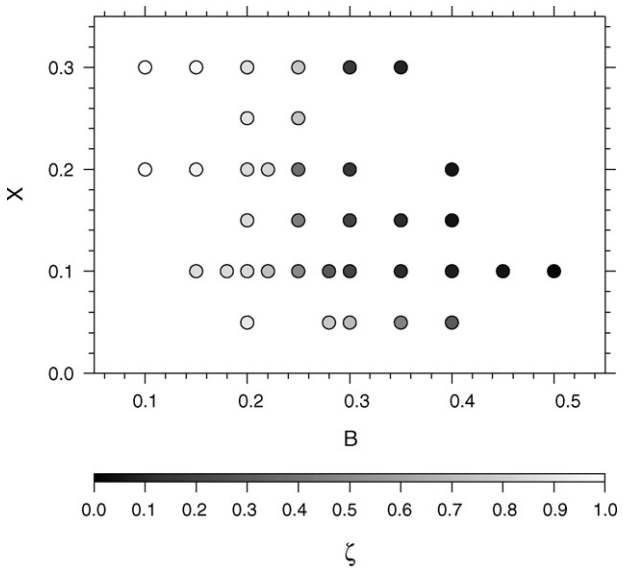

Fig. 11. Normalized time average of the average depth of dense material, ζ (Eq. (7)), as a function of the Buoyancy ratio, B, and the fraction of dense material, X. The value of ζ is denoted by the gray-level scale.

between 40.0 and 210.0 kg/m^3 close to the surface, and between 64.0 and 320.0 kg/m^3 at the bottom of the system. As expected, we observed major changes in the flow pattern and mixing efficiency depending on B.

For buoyancy ratio less than 0.22, we observe patterns similar to the reference case. The dense layer is unstable, and t_{onset} increases with B (Fig. 8a). After the onset of instability, large thermo-chemical plumes develop and remain active for short interval of time ($\delta t \sim 10^{-3}$). Dense and regular materials quickly mix (Fig. 8d), and consequently, the power spectra of chemical density anomalies do not fit those from probabilistic tomography in the long term (Fig. 9). Note that the thermal plumes remain present and stay at the same location during the entire run.

For buoyancy ratio between 0.25 and 0.35, on the contrary, the dense layer does not participate actively to convection. Rather, thermal plumes that rise from its top induce some thermal erosion that entrains dense material upwards. Thermal plumes are smaller and more numerous than in the reference case, and they are interconnected by hot ridges (Fig. 10, plots c and d). Again, in agreement with analogical experiments (Jellinek and Manga, 2002), we observe that the location of these thermal plumes does not vary during the run. As expected, the efficiency of thermal erosion decreases with increasing B (Fig. 8c; see also the evolution of $\langle h_C \rangle$ for $B = 0.25$ and 0.30 in Fig. 8a). Because it is mainly controlled by convection in the layer of regular material, $\langle \text{RMS}(v) \rangle_t$ velocity does not vary much

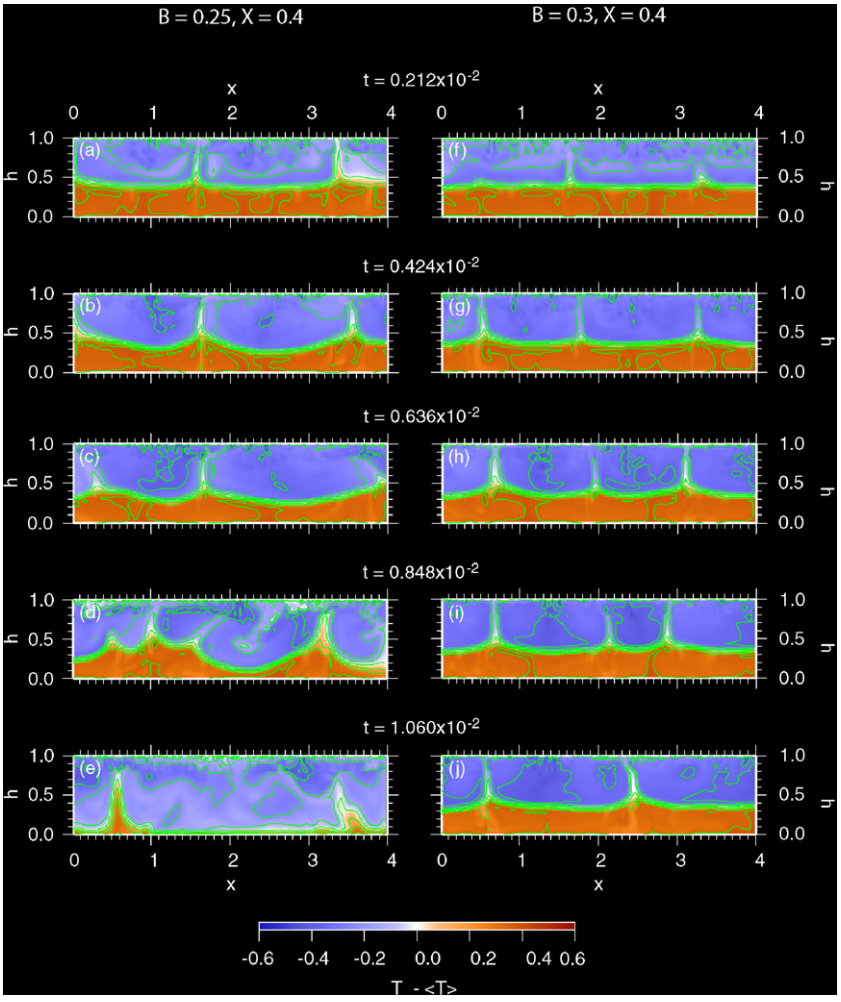

Fig. 12. 2D-slices of the temperature residual, $T - \langle T \rangle$, at different times, and for two cases. Temperature residuals are plotted with both a color scale and contour levels (green curves, interval is 0.1). (a–e) $B = 0.25$ and $X = 0.4$. (f–j) $B = 0.3$ and $X = 0.4$. (For interpretation of the references to color in this figure legend, the reader is referred to the web version of the article.)

with B (Fig. 8d). At large time, thermal erosion results in holes in the layer of dense material (Fig. 10, plots a and b). This induces strong chemical density anomalies up to large ($k=4$) wave number at the bottom of the system ($z \geq 0.85$) (Fig. 10e). As a result, the power spectra of density anomalies in this layer (Fig. 9, 3rd row) fit well those from probabilistic tomography. On the contrary, because most of the dense material remains in the lowermost part of the system, power spectra in the intermediate and upper layers strongly disagree with probabilistic tomography at any time of the run.

Finally, for buoyancy ratio larger than 0.35, the layer of dense material remains stable during the entire run (Fig. 10, plots g and h). Thermal erosion is also present, but does not entrain enough dense material to create holes in the initial dense layer. The average altitude of dense material thus remains around 0.05 during the whole run (Fig. 8a), and strong chemical density anomalies localized at the top of the dense layer (Fig. 10k). Plots g and k in Fig. 10 indicate that the topography of the top of the dense layer is not negligible, around $\delta h = 0.1$. Topography is of course correlated with the hot ridges and the base of thermal plumes. This pattern is very similar to that we observe by increasing the chemical density contrast (Deschamps and Tackley, 2008) except that thermal plumes are larger, and that there is more topography at the top of the layer of dense material.

Clearly, the buoyancy ratio has a dominant role on the flow pattern and on the efficiency of mixing. Large (≥ 0.25) buoyancy ratios induce stable layering. Thermal erosion creates moderate topography, which, if buoyancy ratio is not too high, results in holes in the dense layer, but most of the chemical density anomalies are localized in the lowermost part of the system. Another interesting observation, in agreement with analogical experiments (Jellinek

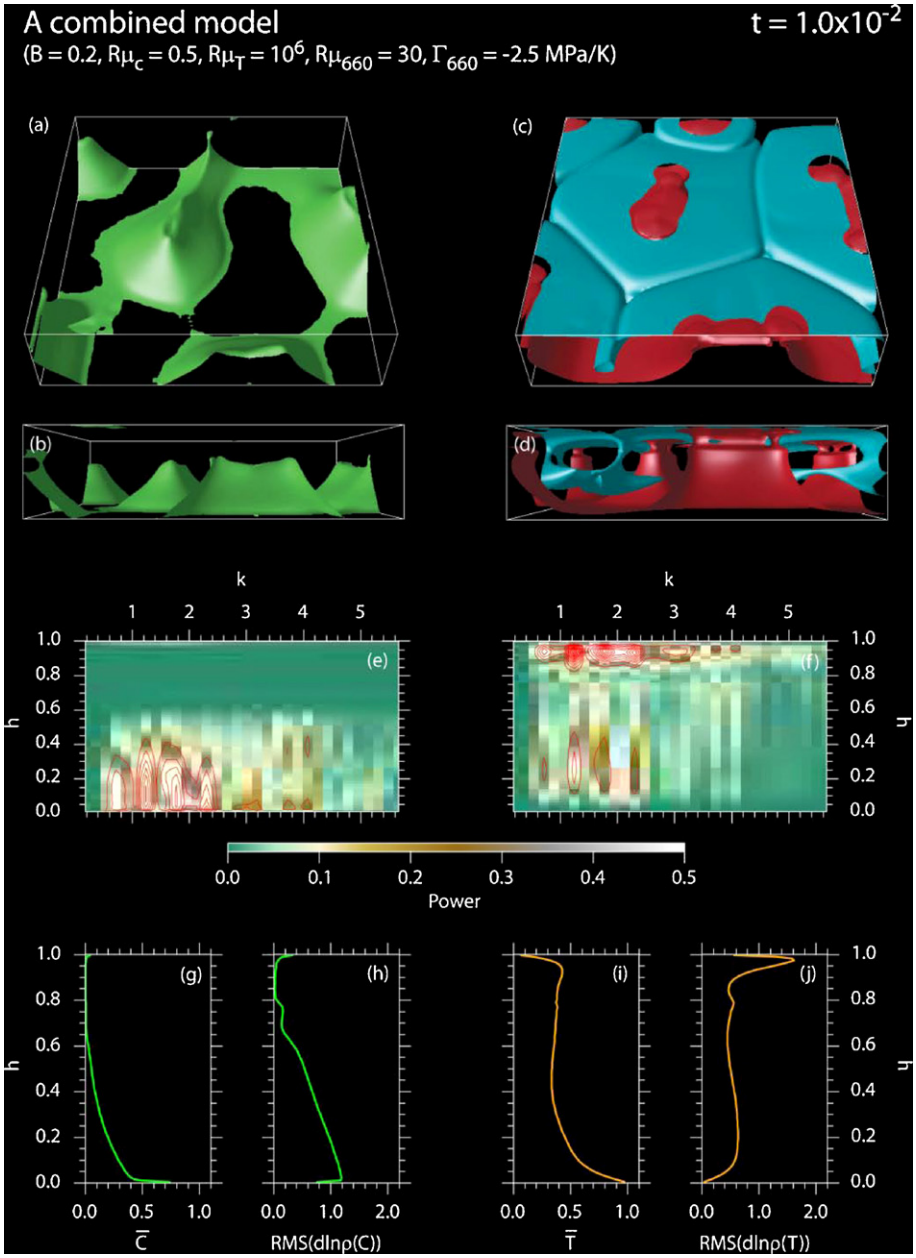

Fig. 13. Snapshot at time $t = 1.0 \times 10^{-2}$ (4.2 Gyr) of a model that combines important ingredients for mantle convection: $B = 0.2$, $R\mu_c = 0.5$, $R\mu_T = 10^6$, $R\mu_{660} = 30$, and $\Gamma_{660} = -2.5$ MPa/K (i.e., a non-dimensional value of -6.68×10^{-2}). Other parameters are as in the reference case: $Ra_S = 10^8$, $H_C = 25$, and $X = 10\%$. Plots description is similar to that in Fig. 6. In plots (c) and (d), contour levels for temperature isosurfaces are $T - \langle T \rangle = -0.225$ (blue) and $T - \langle T \rangle = 0.15$ (red). (For interpretation of the references to color in this figure legend, the reader is referred to the web version of the article.)

and Manga, 2002), is that the thermal plumes are spatially fixed whatever the value of B. More generally, this feature is also observed when additional complexities (e.g., the 660-km phase transition, compositional and thermal viscosity contrasts) are accounted for in the models.

4.2. Fraction of dense material

Finally, we considered values of the volume fraction of dense material, X, between 5 and 30%. Fig. 11, which plots the normalized time average of the mean altitude of dense material (ζ, Eq. (7)) as a function of B and X, suggests that the effect of X is of secondary order compared to that of B.

For $B \leq 0.2$, the dense layer is getting unstable for all the values of X we considered, and the efficiency of mixing varies very little with X. On the contrary, for $B \geq 0.3$ the density contrast is strong enough to prevent the dense layer from getting unstable. In the case $B = 0.3$ and $X = 0.3$, for instance, the layer of dense material remains present during the entire run (unlike the case $B = 0.3$ and $X = 0.1$, Fig. 10, plots a and b, thermal erosion is not efficient enough to create some holes). Additional experiments (not plotted in Fig. 11) for $B = 0.3$ and 0.4 show that the layer is still stable for $X = 50\%$. For intermediate values of the buoyancy ratio (e.g., $B = 0.25$), we observe a regime change around $X = 0.2$–0.25. For $X \leq 0.2$, mixing results from thermal erosion, and ζ is in the range 0.4–0.5. On the contrary, for $X \geq 0.25$, the dense layer breaks up and starts to mix with the regular material. ζ is around 0.75, i.e., the mixing is more efficient than for the cases with $X \leq 0.2$.

A possible explanation of these results is that there exists a critical thickness (or equivalently, fraction of dense material) for which the dense layer switches from a passive mode (thermal erosion) to an active mode, i.e., it is unstable with respect to convection and the whole system convects in two layers. In this later mode, convection of the dense layer induces topography at the interface between the dense and regular material, with an amplitude that depends on the density contrast between the dense and regular material. For small and moderate density contrasts ($B \leq 0.25$), large topography is generated, the dense layer breaks up after a lapse of time that depends on B, dense and regular material mix, and by the end of the run the whole system convects in one layer (Fig. 12a–e). On the contrary, for larger buoyancy ratio ($B \geq 0.3$), topography is weaker, and two-layered convection is maintained during the entire run (Fig. 12f–j).

The value of the critical thickness of the dense layer depends on the model setup (including, in particular, the viscosity law, the buoyancy ratio, the radial model of thermal expansion, and the initial condition), and may be estimated by plotting the Rayleigh number of the dense layer, Ra_{DL}, as a function of the thickness of the dense layer, h_{DL}. Because of our model setup, comparisons of Ra_{DL} against published values of the critical Rayleigh number are however not straightforward. First, the bottom boundary is free-slip, but no condition is applied on the top one (the interface between dense and regular material). Furthermore, our calculations include depth dependent viscosity and mixed heating, for which there is, to our knowledge, no published analytical solution. An accurate determination of the critical Rayleigh number (or equivalently, of the critical thickness of the dense layer) for this configuration thus requires a detailed quantitative study, which is beyond the scope of this paper.

Again, it should be pointed out that the efficiency of mixing mainly depends on the buoyancy ratio. The fraction of dense material is controlling the internal stability of the dense layer, but compared to the buoyancy ratio it has a limited influence on the mixing between dense and regular material. This conclusion is in

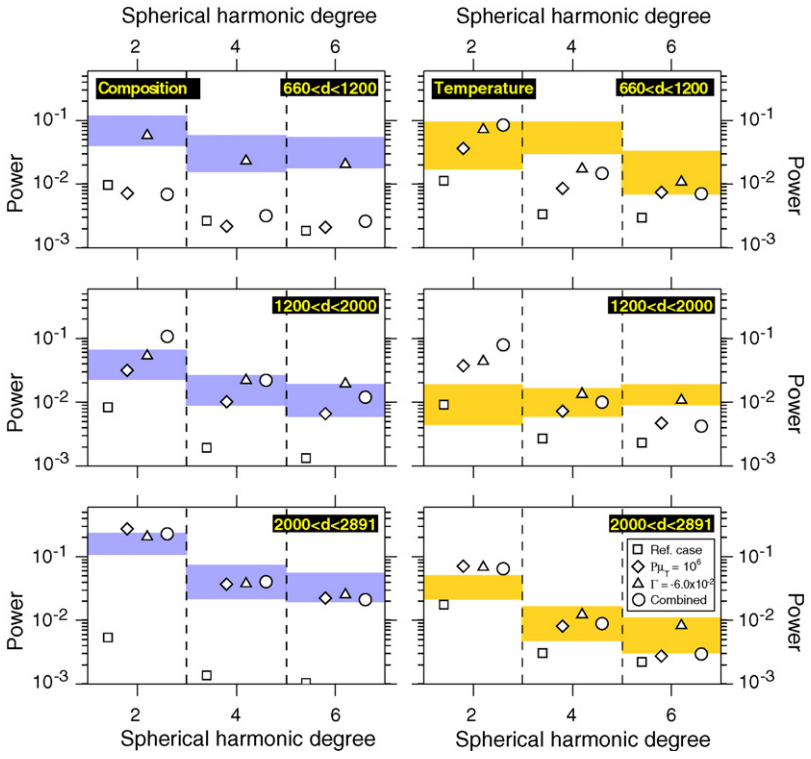

Fig. 14. Power spectra of chemical (left column) and thermal (right column) density anomalies by the end of the run and for various cases. Anomalies are averaged within three layers ($660 \leq d \leq 1200$ km, $1200 \leq d \leq 2000$ km, and $2000 \leq d \leq 2891$ km), and we considered three spherical harmonics ($L = 2$, 4, and 6). Power spectra are further averaged in time in the period range 0.85×10^{-2} to 1.06×10^{-2} (3.5–4.5 Gyr). Gray bands indicate the power spectrum predicted by RT246g within twice its standard deviation. The squares are for the reference case, the diamonds for the case $R\mu_T = 10^6$, the triangles for the $\Gamma_{660} = -2.3$ MPa/K (i.e., a non-dimensional value of -6.0×10^{-2}), and the circles for the combined case discussed in Section 5 ($B = 0.2$, $R\mu_c = 0.5$, $R\mu_T = 10^6$, $R\mu_{660} = 30$, and $\Gamma_{660} = -2.5$ MPa/K).

good agreement with the analogue experiments of Jaupart et al. (2007).

5. Mantle convection: important ingredients

The extensive search in the model space of thermo-chemical we conducted (Deschamps and Tackley, 2008; this paper) can be summarized with five main conclusions, which may be useful to keep in mind when building a thermo-chemical model for the Earth mantle. (1) Large ($\geq$0.3) buoyancy ratios induce stable layering (this paper). For buoyancy ratio between 0.15 and 0.25 (i.e., using the scalings in Table 1, a chemical density contrasts in the range 90–160 kg/m^3 at the bottom of the system), dense material is entrained upwards and, if no other ingredient is added, rapidly mixes with regular material. (2) Small chemical viscosity contrasts induce rapid mixing, whereas large chemical viscosity contrasts lead to stable layering (companion paper). (3) Large ($\geq 10^4$) thermal viscosity contrasts creates pools of dense material with large topography at the bottom of the system. These structures remain stable in time and space. (4) A 660-km viscosity contrast of 30 or more at 660-km depth reduce the mass transfer around this depth (companion paper). (5) An endothermic phase transition at 660-km (with a Clapeyron slope around −3.0 to −1.5 MPa/K) strongly inhibits the rise of dense material above the phase transition. Interestingly, these later two parameters still allow the penetration of downwellings in the lower mantle. In addition to these main conclusions, it is important to note that reducing the Rayleigh number by a factor 3 compared to its assumed value (which is not unreasonable given the uncertainties in upper mantle viscosity, thermal expansion and thermal diffusivity) also contribute to maintain compositional anomalies in the lower mantle during a long period of time.

To test whether a combination of the ingredients discussed in the previous paragraph can explain the observed tomography, we conducted an additional experiment with the following properties: $B = 0.2$, $R\mu_c = 0.5$, $R\mu_T = 10^6$, $R\mu_{660} = 30$, and $\Gamma_{660} = -6.68 \times 10^{-2}$ (−2.5 MPa/K). Fig. 13 shows a snapshot of this experiment by the end of the run ($t = 10^{-2}$, corresponding to a dimensional time of 4.2 Gyr). Large pools of dense material rise from the bottom of the system up to the 660-km transition (Fig. 13, plots a and b). They induce strong chemical density anomalies with wave number up to $k = 2.5$ (Fig. 13e) and increasing amplitude with depth (Fig. 13h). Due to the value of the Clapeyron slope of the 660-km transition, a very small amount of dense material penetrates in the upper mantle. Large hot plumes also rise from the bottom of the mantle, but the combined actions of the 660-km viscosity contrast and endothermic phase transition considerably thin them as they enter the upper mantle (Fig. 13, plots c and d). Note that unlike cases that account for the phase transition only (Fig. 6), thermal plumes

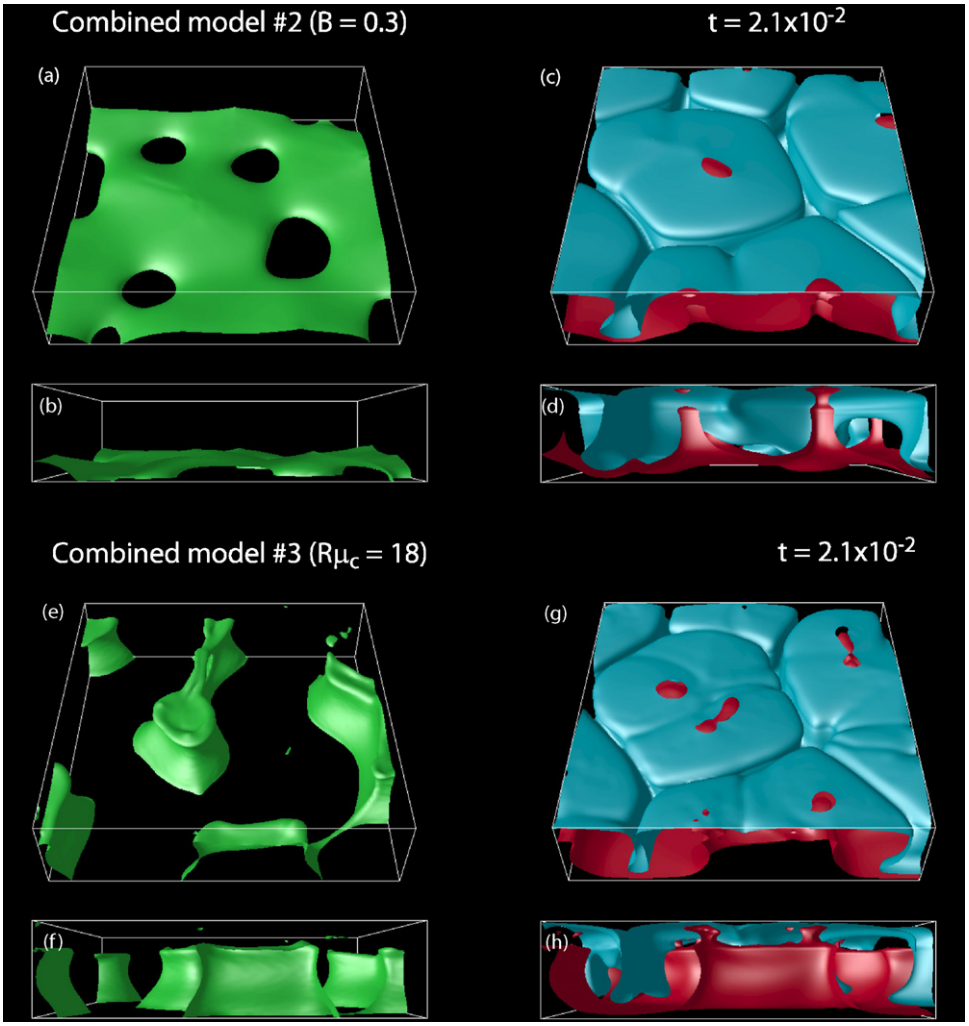

Fig. 15. Snapshots at time $t = 2.12 \times 10^{-2}$ (9.0 Gyr) for two additional models with $R\mu_T = 10^6$, $R\mu_{660} = 30$, and $\Gamma_{660} = -2.5$ MPa/K. (a–d) $B = 0.3$ and $R\mu_c = 0.5$. (e–h) $B = 0.2$ and $R\mu_c = 18$. Plots description is similar to that in plots (a–d) of Fig. 6. In plots (c) and (d), contour levels for temperature isosurfaces are $T - \langle T \rangle = -0.15$ (blue) and $T - \langle T \rangle = 0.15$ (red), respectively. In plots g and h, contour levels for temperature isosurfaces are $T - \langle T \rangle = -0.2$ (blue) and $T - \langle T \rangle = 0.15$ (red), respectively. (For interpretation of the references to color in this figure legend, the reader is referred to the web version of the article.)

are not stopped but only thinned (Fig. 13d; see also the temperature profile, Fig. 13i, which do not show a sharp increase around 660-km depth). Downwellings, by contrast, penetrate more easily in the lower mantle. The thinned plumes and the downwellings induce strong thermal density anomalies in a layer that extends from the surface down to $z \sim 0.1$ ($\sim$300-km depth) (Fig. 13, plots f and j). Interestingly, these thermo-chemical structures are long lived. Extending the calculations up to time $t = 0.0212$ (9.0 Gyr), we observe that they are still present. Furthermore, the power spectrum of density anomalies predicted by this model is in excellent agreement with that from probabilistic tomography, except in the layer 660–1200 km (open circles in Fig. 14). A possible explanation for this disagreement is that the anomalies observed by probabilistic tomography in this layer are related to accumulation of slabs around the 660-km boundary. Because we assumed two types of particles only (for regular and dense material, the dense material being initially concentrated in basal layer), our treatment of the chemical field does not account for the effects of downwellings on the distribution of chemical density anomalies. To achieve this, more complex modeling including a third type of particle and the generation of MORB and harzburgite materials from an initial mantle reservoir and their recycling in the deep mantle, is needed. It is however interesting to note that the thermal density anomalies fit well those from probabilistic tomography (right row in Fig. 14), which might be the thermal signature of slabs. Alternatively, anomalies in this layer may be due to dense material that remains trapped below the phase transition, as one would expect for a Clapeyron slope around -2.3 MPa/K (-6.0×10^{-2}) and a viscosity that is not temperature-dependent (Fig. 6b, and top row in Fig. 7).

Finally, we run additional cases to investigate the relative importance of the chemical density and viscosity contrasts for models that include large thermal viscosity contrasts and a negative Clapeyron slope at 660 km. These additional models have properties similar to those of the combined model, except that we prescribed either another value of the buoyancy ratio, or another value of the chemical viscosity contrast. First, we run a model with a buoyancy ratio $B = 0.3$ (plots a–d in Fig. 15; note that this snapshop is taken at $t = 0.0212$). Clearly, the layer of dense material remains stable for long period of time and experiences thermal erosion, which generates structures alike those observe in Fig. 9a–d. The density contrast is therefore a first order controlling parameter, and to avoid stable layering, the buoyancy ratio should not be fixed to more than 0.25. In a second case, we fixed the chemical viscosity contrast to $R\mu_c = 18$, and found that the layer of dense material remains stable until $t = 0.0106$ (4.5 Gyr). However, if calculation is continued further in time, large piles of dense material are generated (Fig. 15e–h). Although narrower, these structures resemble those observed in the combined case (in particular, note that the piles are blocked below the 660-km phase transition), and explain probabilistic tomography well. We obtained a similar results for $R\mu_c = 32$, but for $R\mu_c = 64$ we observe chemical structures alike those obtained for moderate $R\mu_c$ and $R\mu_T = 1$ (companion paper, Fig. 4g–h), and for $R\mu_c = 10^2$ we observed stable layering with moderate topography. In these models, the strong thermal viscosity contrast compensates the chemical increase in viscosity (up to values of $R\mu_c$ around 50), and allows dense material to rise. In a last experiment, we considered a small chemical viscosity contrast ($R\mu_c = 10^{-2}$), and found thermo-chemical structures similar to those of the combined case. Thus, the range of chemical viscosity contrast for which large pools of dense material can be maintained depends on the thermal viscosity contrast. Models that include large thermal viscosity contrast may support larger chemical contrasts (typically up to about 50 for $R\mu_T = 10^6$) than models with low or moderate values of $R\mu_T$. A more extensive study should conducted be to better map this relationship.

6. Concluding remarks

Our search for successful dynamic models of Earth's mantle was essentially based on comparison between models of thermo-chemical convection and a tomographic model that include estimates of density distribution, which play a crucial role in resolving the trade-off between temperature and composition. To give more support to our findings, it is important to estimate possible Earth mantle values of the model parameters we discussed from available geophysical constraints. (1) First, one may estimate possible values of buoyancy ratio assuming that the density excess at the bottom of the mantle is related to the presence of iron-rich post-perovskite. Assuming that the average mantle composition is pyrolitic (Si/Mg $\sim$0.8 and Fe/Mg $\sim$0.11), and using available data for post-perovskite (Tsuchiya et al., 2004) and an appropriate equation of state modeling (Deschamps and Trampert, 2004), we find that a 2.0–3.0% excess in the volume fraction of iron in the lowermost mantle (Trampert et al., 2004) may result in a chemical density contrast between 90 and 130 kg/m^3. Assuming a thermal density contrast in the lower part of the system equal to $\Delta\rho_{LS} = 625.0$ kg/m^3 (corresponding to an average density in the $\rho_{LS} = 5000$ kg/m^3), this lead to a buoyancy ratio between 0.14 and 0.21. (2) To date, very few data concerning the viscosity of post-perovskite and the iron end-members of mantle minerals are available, and it is difficult to make reasonable estimates of the compositional viscosity contrast. (3) The viscosity of mantle aggregate is clearly temperature-dependent, and this dependence is well explained by an Arrhenius type of law. Taking a mantle adiabat and a super-adiabatic temperature difference equal to $T_{as} = 1200\,^\circ$C and $\Delta T = 2500$ K, respectively, a thermal viscosity contrast in the range 10^5–10^7 would correspond to a thermal activation energy between 220 and 310 kJ/mol. These values are consistent with mineral physics data for the activation energies of perovskite and magnesio-wüstite (Yamazaki and Karato, 2001). (4) Estimates of the 660-km viscosity jump from various geophysical observations are also available (e.g., Hager and Richards, 1989; Nakada and Lambeck, 1989; Forte and Mitrovica, 1996), and our preferred range of values for this viscosity contrast (10–30) is consistent with the observed values. (5) Finally, the transformation of ringwoodite into perovskite and magnesio-wüstite is endothermic, with Clapeyron slope between -3.0 and -2.0 MPa/K (Bina and Helffrich, 1994). Note that the transformation of garnet may modify the effective Clapeyron slope at $z = 660$ km (see discussion below). Overall, the ingredients we identified are in very good agreement with available independent geophysical data.

Our models also predict surface heat flow, Φ_{surf}, average temperature of the upper mantle ($200 \le d \le 660$ km), T_{UM}, and surface velocity, V_{surf}, that we can compare with values observed for the Earth. Table 2 lists the time-average (over the last Gyr for of the run) of these parameters for selected models of thermo-chemical convection. Heat flow values may be compared against that of the compilation of Pollack et al. (1993). One must however keep in mind that the observed surface heat flow is likely overestimating the heat flow at the top of the mantle. The reason is that the measured surface heat flow includes a contribution related to crustal heat production, which is difficult to estimate. In cratonic regions, this contribution may be large and the mantle heat flux could be as low as 15–20 mW/m^2 (Jaupart and Mareschal, 2007). Comparisons between the surface heat flow predicted by our models and the observed ones may thus be helpless to discriminate among possible models. Classical value for the average temperature the upper mantle is in the range 1200–1400 K. Both Φ_{surf} and T_{UM} decrease with increasing buoyancy ratio and increasing absolute value of the Clapeyron slope. This decrease is more pronounced for $\Gamma_{660} \le -1.5$ MPa/K (-4.0×10^{-2}), and for $\Gamma_{660} = -3.0$ MPa/K (-8.0×10^{-2}) the calculated Φ_{surf} and T_{UM} are difficult to reconcile

Table 2
Predicted upper mantle potential temperature, surface heat flow, and RMS of surface velocity for selected cases[a].

Case	T_{UM} (K)[b]	Φ_{surf} (mW/m^2)[c]	RMS(v_{surf}) (cm/year)
Reference case	970	77.5	3.1
$Ra_S = 3.0 \times 10^7$	1080	66.7	1.4
$Ra_S = 3.0 \times 10^8$	760	74.1	4.9
$\Gamma_{660} = 0.76$ MPa/K[d]	960	76.4	3.3
$\Gamma_{660} = 1.53$ MPa/K	950	74.9	2.3
$\Gamma_{660} = 3.06$ MPa/K	650	33.8	1.4
$B = 0.15$	950	82.0	3.4
$B = 0.25$	930	71.0	2.4
$B = 0.40$	840	55.1	2.0
Combined case[e]	1230	45.8	0.6

[a] Average values over the last Gyr of the run. Possible values for the Earth upper mantle temperature are in the range 1200–1400 K. Surface heat flow strongly varies with location. The compilation of Pollack et al. (1993) proposes a global value around 87 mW/m^2, with oceanic and continental values around 101 and 65 mW/m^2, respectively.

[b] The upper mantle potential temperature is averaged in the layer $200 \le d \le 660$ km ($0.07 \le z \le 0.228$), and scaled with a super-adiabatic temperature difference $\Delta T_S = 2500$ K and a surface temperature $T_{surf} = 300$ K. The real temperature can be estimated by assuming that the adiabatic gradient in this layer is 0.4 K/km, i.e., by adding an adiabatic contribution of about 100 K.

[c] Surface heat flow includes a contribution from the adiabatic gradient of temperature. In the reference state we used (Tackley, 1996, 1998a), the adiabatic gradient below the surface gradient is about 0.8 K/km. Taking $k_S = 3.0$ W m^{-1} K^{-1}, the adiabatic contribution to the surface heat flow is thus 2.4 mW/m^2.

[d] Non-dimensional Clapeyron slopes are -0.2×10^{-1}, -0.4×10^{-1}, and -0.8×10^{-1}, respectively.

[e] Combined case properties are $Ra_S = 10^8$, $B = 0.2$, $X = 10\%$, $R\mu_c = 0.5$, $R\mu_{660} = 30$, $R\mu_z = 10$, $R\mu_T = 10^6$, and $\Gamma_{660} = -2.5$ MPa/K (i.e., a non-dimensional value of -6.68×10^{-1}).

with the observed surface heat flow and the upper mantle adiabat. For the combined case, the predicted upper mantle temperature is comparable to that expected for the Earth's upper mantle, but the predicted heat flux is low (45.8 mW/m^2) compared to the global average heat flow (87 mW/m^2, Pollack et al., 1993). Again, this disagreement may be partly explained by the fact that the observed surface heat flow is not corrected from the crustal heat production and is thus higher than the actual heat flow coming out of the mantle. Except for the combined case, the models listed in Table 2 do not include lateral variations of viscosity, and thus the horizontal velocity is fully poloidal. For the Earth, the ratio between toroidal and poloidal velocities is around 0.4–0.6 (Lithgow-Bertelloni et al., 1993; Becker, 2006), and the average surface poloidal velocity is typically in the range 2–6 cm/year. In our models, the surface velocity decreases with both the buoyancy ratio and the amplitude of the Clapeyron slope, but remains close to the typical value for the Earth. Unsurprisingly, V_{surf} increases with the Rayleigh number. Note that for Ra_S around 3.0×10^7 and less, V_{surf} is too small compared to the observed values for the Earth. Due to the large value of the thermal viscosity ratio, which increases the rigidity of the fluid close the surface, the surface velocity predicted by the combined case is small, less than 1 cm/year. Note that the presence of additional ingredients prevent the combined case to fit in the conductive-lid regime observed for strongly temperature-dependent viscosity fluid (e.g., Davaille and Jaupart, 1993; Moresi and Solomatov, 1995). The disagreement between the surface velocity predicted by the combined case and the observed one may be fixed by imposing an appropriate rheology at the top of the fluid to model that would properly models the lithosphere (Tackley, 1998b, 2000).

The role of the phase transition at $d = 660$ km is of particular importance. Clearly, downwellings can penetrate below this transition. In agreement with purely thermal convection models (Tackley et al., 1993, 1994), we observe that avalanches occur at any time, but not necessarily at the same location. This is consistent with tomographic images, which show that slabs can either sink into the deep mantle or stack around 1000-km depth (van der Hilst et al., 1997; Fukao et al., 2001). By contrast, the large hot plumes that rise from the bottom thermal boundary layer are strongly inhibited as they cross the 660-km phase transition and, if temperature-dependent viscosity is not accounted for, they even stopped below it. Upward mass transfer is strongly inhibited, and most of the dense material remains trapped in the lower mantle. Interestingly, this observation gives support to the existence of a buried reservoir enriched in dense material in the lower mantle. The existence of two reservoirs in the mantle (a pyrolitic reservoir and a reservoir enriched in dense material) is often advocated to explain geochemical differences observed between OIB and MORB materials (e.g., Zindler and Hart, 1986; Hofmann, 1997). Possible origins for the reservoir enriched in dense material include a subducted early crust (Boyet and Carlson, 2006), and the formation and crystallization of a magma ocean at the bottom of the mantle (Labrosse et al., 2007). The original shape of the dense reservoir is unknown, but it may have evolved to disconnected piles or pools of dense material, which are presently responsible for large regions of low shear-wave velocity anomalies observed at the bottom of the mantle (e.g., Lay et al., 2004; Trampert et al., 2004; Deschamps et al., 2007; Garnero et al., 2007). The presence (eventually as a remnant of an initial magma ocean) of partially molten material at the base of these piles may explain the Ultra Low Velocity Zone locally observed at the bottom of the mantle (see Thorne and Garnero, 2004 for a recent review).

The 660-km phase transition was modeled with a single Clapeyron slope imposed around $d = 660$ km. The real Earth is however thermodynamically more complex, with various minerals transforming at different depths and with different Clapeyron slopes. Garnets, for instance, transform at greater depth than Ringwoodite, around 710 km (e.g., Stixrude, 1997). It is thus an oversimplification to model the 660-km phase chemical change with a single endothermic phase transition. Accounting for the full phase diagram in this depth-range may have strong implications in the flow pattern and in the distribution of density anomalies. More generally, multiphase models of mantle convection may have important consequences for mantle dynamics and heat transfer (Nakagawa and Tackley, 2005a). In addition, the post-perovskite phase transition at the bottom of the system, which is not included in our model, may have some specific signatures. It has been pointed out, for instance, that the distributions of dense material and post-perovskite are anti-correlated (Nakagawa and Tackley, 2005b, 2006), and that the spectra of chemical anomalies are strongly influenced by the topography of the post-perovskite phase transition (Nakagawa and Tackley, 2006). Note that the seismological evidences for the presence of post-perovskite at the base of the mantle are not fully conclusive and indicate that D'' is likely more complex than a post-perovskite layer (Lay and Garnero, 2007). This may in turn influence the dynamics of the mantle.

Other limitations of our approach and models were discussed in our companion paper. They include the lack of sources and sinks of dense material, which may slightly bias our results. Accounting for sources and sinks of dense material may for instance allow the creation and recycling of MORB material. More importantly, spherical geometry modifies the stability of top and bottom thermal boundary layers, and may strongly affect the flow pattern and the stability a basal layer of dense material. In particular, sphericity increases the stability of the bottom thermal boundary layer, and the ingredients that stabilize the layer of dense material (large compositional viscosity and density contrasts) are likely to have stronger effects.

Our search in the model space of thermo-chemical convection considered relatively simple models, and, as discussed above, additional complexities should be included to produce more realistic models that may explain geophysical observations in more details. Our approach, however, allowed identification of important ingredients that may enter a first order model of Earth's mantle dynamics: a moderate chemical density contrast; a large thermal

viscosity contrast; a viscosity jump at 660-km of about 30; and a Clapeyron slope of the 660-km phase transition around −3.0 to −1.5 MPa/K. When included in a single model, these ingredients create and maintain thermo-chemical structures that explain well the thermo-chemical distributions predicted by probabilistic tomography. Finally, for models that include a large thermal viscosity contrast, the chemical viscosity contrast has only a limited influence on the formation and survival of large thermo-chemical pools. However, the detailed structure of these pools significantly depends on the chemical viscosity contrast, and comparisons against tomographic models with vertical and lateral resolution better than those of the present probabilistic tomography may be able discriminate among these structures.

Acknowledgments

We are grateful to Allen McNamara and an anonymous colleague for their constructive reviews that helped to clarify some parts of this paper.

References

Bina, C.R., Helffrich, G., 1994. Phase transitions Clapeyron slopes and transition zone seismic discontinuity tomography. J. Geophys. Res. 99, 15853–15860.
Becker, T.W., 2006. On the effect of temperature and strain-rate dependent viscosity on global mantle flow, net rotation, and plate driving forces. Geophys. J. Int. 167, 943–957.
Boyet, M., Carlson, R.W., 2006. ^{142}Nd evidence for early (>4.53 Ga) global differentiation of the silicate Earth. Science 309, 576–581.
Chevrot, S., Montagner, J.-P., Snieder, R., 1998. The spectrum of tomographic Earth models. Geophys. J. Int. 133, 783–788.
Christensen, U.R., Yuen, D.A., 1985. Layered convection induced by phase transitions. J. Geophys. Res. 90, 10291–10300.
Coltice, N., 2005. The role of convective mixing in degassing the Earth's mantle. Earth Planet. Sci. Lett. 234, 15–25.
Davaille, 1999. Simultaneous generation of hotspots and superswells by convection in a heterogeneous planetary mantle. Nature 402, 756–760.
Davaille, A., Jaupart, C., 1993. Transient high-Rayleigh number thermal convection with large viscosity variations. J. Fluid Mech. 253, 141–166.
Deschamps, F., Trampert, J., 2003. Mantle tomography and its relation to temperature and composition. Phys. Earth Planet. Inter. 140, 277–291.
Deschamps, F., Trampert, J., 2004. Towards a lower mantle reference temperature and composition. Earth Planet. Sci. Lett. 222, 161–175.
Deschamps, F., Trampert, J., Tackley, P.J., 2007. Thermo-chemical structure of the lower mantle: seismological evidence and consequences for geodynamics. In: Yuen, D.A., et al. (Eds.), Superplumes: Beyond Plate Tectonics. Springer, pp. 293–320.
Deschamps, F., Tackley, P.J., 2008. Exploring the model space of thermo-chemical convection I–Principles and influence of the rheological parameters. Phys. Earth Planet. Inter. 171, 357–373.
Forte, A.M., Mitrovica, J.X., 1996. New inferences of mantle viscosity from joint inversion of long-wavelength mantle convection and post-glacial rebound data. Geophys. Res. Lett. 23, 1050–1147.
Fukao, Y., Widiyantoro, S., Obayashi, M., 2001. Stagnant slabs in the upper and lower mantle transition region. Rev. Geophys. 39, 291–323.
Garnero, E.J., Thorne, M.S., McNamara, A., Rost, S., 2007. Fine-scale ultra low velocity zone layering at the core-mantle boundary and superplumes. In: Yuen, D.A., et al. (Eds.), Superplumes: Beyond Plate Tectonics. Springer, pp. 139–157.
Hager, B.H., Richards, M.A., 1989. Long-wavelength variations in Earth's geoid: physical models and dynamical implications. Philos. Trans. R. Soc. Lond. A 328, 309–327.
Hofmann, A.W., 1997. Mantle geochemistry: the message from oceanic volcanism. Nature 385, 219–229.
Ishii, M., Tromp, J., 1999. Normal-mode and free-air gravity constraints on lateral variations in velocity and density of Earth's mantle. Science 285, 1231–1236.
Jaupart, C., Molnar, P., Cottrell, E., 2007. Instability of a chemically dense layer heated from below and overlain by a deep less viscous fluid. J. Fluid Mech. 572, 433–469.
Jaupart, C., Mareschal, J.-C., 2007. Heat flow and thermal structure of the lithosphere. In: Schubert, G., et al. (Eds.), Treatise on Geophysics, vol. 3: Crust and Lithosphere Dynamics, pp. 218–251.
Jellinek, A.M., Manga, M., 2002. The influence of a chemical boundary layer on the fixity, spacing and lifetime of mantle plumes. Nature 418, 760–763.
Karato, S.-I., Karki, B.B., 2001. Origin of lateral variation of seismic wave velocity and density in the deep mantle. J. Geophys. Res. 106, 21771–21783.
Katsura, T., Ito, E., 1989. The system Mg_2–SiO_4–Fe_2–SiO_4 at high pressures and temperatures: precises determination of stabilities of olivine, modified spinel, and spinel. J. Geophys. Res. 94, 15663–15670.
Labrosse, S., Hernlund, J.W., Coltice, N., 2007. A crystallizing dense magma ocean et the base of the Earth's mantle. Nature 450, 866–869.
Lay, T., Garnero, E.J., Williams, Q., 2004. Partial melting in a thermo-chemical boundary layer at the base of the mantle. Phys. Earth Planet. Inter. 146, 441–467.
Lay, T., Garnero, E.J., 2007. Reconciling the post-perovskite phase with phase transition with seismological observations of lowermost mantle structure. In: Hirose, K., et al. (Eds.), Post-perovskite the Last Mantle Phase Transition, Geophys. Monograph, vol. 174, pp. 129–153.
Lithgow-Bertelloni, C., Richards, M.A., Ricard, Y., O'Connell, R.J., Engebretson, D.J., 1993. Toroidal–poloidal partitioning of plate motion since 120 Ma. Geophys. Res. Lett. 20, 375–378.
Machetel, P., Weber, P., 1991. Intermittent layered convection in a model mantle with an endothermic phase change at 670 km. Nature 350, 55–57.
Moresi, L.-N., Solomatov, V.S., 1995. Numerical investigation of 2D convection with extremely large viscosity variations. Phys. Fluids 7, 2154–2162.
Nakada, M., Lambeck, K., 1989. Late pleistocene and holocene sea-level change in the Australian region and mantle rheology. Geophys. J. Int. 96, 497–517.
Nakagawa, T., Tackley, P.J., 2005a. Deep mantle heat flow and thermal evolution of Earth's core in thermo-chemical multiphase models of mantle convection. Geochem. Geophys. Geosyst. 6, doi:10.1029/2005GC000967.
Nakagawa, T., Tackley, P.J., 2005b. The interaction between the post-perovskite phase change and a thermo-chemical boundary layer near the core-mantle boundary. Earth Planet. Sci. Lett. 238, 204–216.
Nakagawa, T., Tackley, P.J., 2006. Three-dimensional structures and dynamics in the deep mantle: effects of post-perovskite phase change and deep mantle layering. Geophys. Res. Lett. 33, doi:10.1029/2006GL025719.
McNamara, A.K., Zhong, S., 2004. Thermochemical structures within a spherical mantle. J. Geophys. Res. 109, doi:10.1029/2003JB002847.
McNamara, A.K., Zhong, S., 2005. Degree-one mantle convection: dependence on internal heating and temperature-dependent rheology. Geophys. Res. Lett. 32, doi:10.1029/2004GL021082.
Pollack, H.N., Hurter, S.J., Johnson, J.R., 1993. Heat flow from the earth interior: analysis of global data set. Rev. Geophys. 31, 267–280.
Saltzer, R.L., van der Hilst, R.D., Kárason, H., 2001. Comparing P and S wave heterogeneity in the mantle. Geophys. Res. Lett. 28, 1335–1338.
Solheim, L.P., Peltier, W.R., 1994. Phase boundary deflection at 660-km depth and episodically layered isochemical convection in the mantle. J. Geophys. Res. 99, 15861–15875.
Sotin, S., Labrosse, S., 1999. Three-dimensional thermal convection in an iso-viscous, infinite Prandtl number fluid heated from within and from below: applications to the transfer of heat through planetary mantles. Phys. Earth Planet. Inter. 112, 171–190.
Stixrude, L., 1997. Structure and sharpness of phase transitions and mantle discontinuities. J. Geophys. Res. 102, 14835–14852.
Tackley, P.J., 1996. On the ability of phase transitions and viscosity layering to induce long wavelength heterogeneity in the mantle. Geophys. Res. Lett. 23, 1985–1988.
Tackley, P.J., 1998a. Three-dimensional simulations of mantle convection with a thermo-chemical CMB boundary layer: D''? In: Gurnis, M., et al. (Eds.), The Core-Mantle Boundary Region. Geodynamical Ser. 28, pp. 231–253.
Tackley, P.J., 1998b. Self-consistent generation of tectonic plates in three-dimensional mantle convection. Earth Planet. Sci. Lett. 157, 9–22.
Tackley, P.J., 2000. Mantle convection and plate tectonics: towards an integrated physical and chemical theory. Science 288, 2002–2007.
Tackley, P.J., 2002. Strong heterogeneity caused by deep mantle layering. Geochem. Geophys. Geosyst. 3, doi:10.1029/2001GC000167.
Tackley, P.J., King, S.D., 2003. Testing the tracer ratio method for modeling active compositional fields in mantle convection simulations. Geochem. Geophys. Geosyst. 4, doi:10.1029/2001GC000214.
Tackley, P.J., Stevenson, D.J., Glatzmaier, G.A., Schubert, G., 1993. Effect of an endothermic phase transition at 670 km in a spherical model of convection in the Earth's mantle. Nature 361, 699–704.
Tackley, P.J., Stevenson, D.J., Glatzmaier, G.A., Schubert, G., 1994. Effects of multiple phase transitions in three-dimensional spherical model of convection in the Earth's mantle. J. Geophys. Res. 99, 15877–15901.
Thorne, M.S., Garnero, E.J., 2004. Inferences on ultralow-velocity zone structure from a global analysis of SPdKS waves. J. Geophys. Res. 109, B08301, doi:10.1029/2004JB03010.
Trampert, J., Deschamps, F., Resovsky, J.S., Yuen, D.A., 2004. Probabilistic tomography maps significant chemical heterogeneities in the lower mantle. Science 306, 853–856.
Travis, B., Olson, P., 1994. Convection with internal sources and turbulence in the Earth's mantle. Geophys. J. Int. 118, 1–19.
Tsuchiya, T., Tsuchiya, J., Umemoto, K., Wentzcovitch, R.M., 2004. Phase transition in $MgSiO_3$ perovskite in the lower mantle. Earth Planet. Sci. Lett. 224, 241–248.
van der Hilst, R.D., Widiyantoro, S., Engdahl, E.R., 1997. Evidence for deep mantle circulation from seismic tomography. Nature 386, 578–584.
Weinstein, S.A., 1992. Induced compositional layering in a convective fluid layer by an endothermic phase transition. Earth Planet. Sci. Lett. 113, 23–39.
Yamazaki, D., Karato, S.-I., 2001. Some mineral physics constraints on the rheology and geothermal structure of Earth's lower mantle. Am. Mineral. 86, 385–391.
Yuen, D.A., Reuteler, D.M., Balachandar, S., Steinbach, V., Malevsky, A.V., Smedsmo, J.J., 1994. Various influences on three-dimensional mantle convection with phase transition. Phys. Earth Planet. Inter. 86, 185–203.
Zindler, S., Hart, S., 1986. Chemical geodynamics. Annu. Rev. Earth Planet. Sci. 14, 493–571.